Quasi-spherical Direct Drive Fusion

Tom Nash, Pace VanDevender, Dillon McDaniel, Norm Roderick, William Langston, Marisel Silva, and Luke Abbot

![Sandia National Laboratories logo]

Quasi-spherical Direct Drive Fusion Report for LDRD 06-1526

Tom Nash, Pace VanDevender, Dillon McDaniel, Norm Roderick,
William Langston, Marisel Silva, and Luke Abbot
Sandia National Laboratories
Albuquerque NM 87185

ABSTRACT

We present designs of quasi-spherical direct drive z-pinch loads for machines such as ZR at 28 MA load current with a 150 ns implosion time (QSDD1).   A double shell system for ZR has produced a 2D simulated yield of 12 MJ, but the drive for this system on ZR has essentially no margin.   A double shell system for a 56 MA driver at 150 ns implosion has produced a simulated yield of 130 MJ with considerable margin in attaining the necessary temperature and density-radius product for ignition.   We also present designs for a magnetically insulated current amplifier, (MICA), that modify the attainable ZR load current to 36 MA with a 28 ns rise time.   The faster pulse provided by a MICA makes it possible to drive quasi-spherical single shell implosions (QSDD2). We will present results from 1D LASNEX and 2D MACH2 simulations of promising low-adiabat cryogenic QSDD2 capsules and 1D LASNEX results of high-adiabat cryogenic QSDD2 capsules.

Contents

Figures

Tables

I.   INTRODUCTION

Quasi-spherical z-pinch implosions have been investigated in the field of magnetized target fusion (MTF). [1] Typically MTF implosions are over a time frame of a few μs or more. [2] Due to the slow implosion rate, the MTF approach requires that the deuterium-tritium (DT) fuel be magnetized to reduce thermal losses to the high Z quasi-spherical liner. If fast, 100-ns, implosion time quasi-spherical implosions can be realized, then the implosion is fast enough at14 to 30 cm/μs. Thermal losses from an internal fluid to the liner are small, and it is not necessary for the internal fluid to be magnetized.

Quasi-spherical isentropic z-pinch implosions with a shaped current drive have been proposed as an alternate means to produce fusion by preparing high-density DT for fast ignition on Z. [3] Cylindrical z-pinches are also being used as radiation sources for indirectly driving fusion pellets via ablation. [4, 5, 6]

Direct-drive quasi-spherical z-pinch compressions offer several advantages over x-ray ablatively driven pellets as fusion drivers. One advantage is efficiency. Since the quasi-spherical implosion is nearly adiabatic, most of the kinetic energy of the imploding liner is converted into internal energy of the DT fluid. This adiabatic direct process is much more efficient than first converting pinch implosion kinetic energy into radiation, and then using that radiation to ablatively drive a pellet.   The high efficiency of the QSDD1 and QSDD2 approaches lead to reduced requirements on shell convergence for ignition and on required machine parameters. [7, 8]

In this report we present designs for quasi-spherical loads on the 28-MA, 150-ns accelerator ZR, for ZR with the load current amplified via MICA, and for future machines with load current larger than ZR.

Results of 1D simulations of QSDD1 loads driven by a pressure source have been published. [7, 8] Those results indicated that if quasi-spherical z-pinches exhibit enough stability and adequate convergence, volumetric ignition should be possible on machines larger than ZR for both single and double shell systems.   In section II of this report, we present results of 2D QSDD1 simulations driven by a circuit source.   These results indicate that ignition of the inner shell of a QSDD1 double shell system should be possible on machines larger than ZR.

The stability and non-uniform expansion of the imploding shell in a single shell QSDD1 load, as revealed by 2D circuit-source simulations, make achieving ignition in these loads more difficult than in double shell loads.   However MICA technology sharpens and amplifies the current to make driving single shell loads (QSDD2) possible. The MICA stores the energy in an azimuthally propagating wave in multiple, parallel, inwardly spiraling, self Magnetically Insulated Transmission Lines (MITLs) and extracts the energy with multiple parallel switches on the top edge of each MITL to feed energy into a radially converging convolution to a central load.   Since the effective impedance of the wave propagating in the axial direction is much less than the wave impedance propagating in the azimuthal direction, the switching amplifies the current available to

the load. Modest pulse shaping can be obtained by 1) letting the main pulse feed the central load for a first pulse, 2) switching additional energy from the MITLs, and 3) varying the switch timing to fine tune the shape of the second pulse. Destructive and constructive interference of the waves in the MITLs, the inductance of the switches and convolutions, and the potential for breakdown of magnetic insulation all limit the efficiency of the device.

In section III we present the design for a MICA system on ZR.   In section IV, we present results of 1D simulations showing ignition in QSDD2 loads driven by ZR with MICA, and show preliminary results from 2D simulations of QSDD2 z-pinch loads.

II.   QSDD1

For QSDD1 loads we consider loads for 150 ns implosions driven by ZR. Because these implosions are fairly long it would difficult to fabricate full quasi-spherical shells that can be accelerated to a velocity greater than 20 cm/μs needed to heat DT to ignition temperature.   Such complete shells would be too thin to make. However quasi-spherical loads that accelerate to a velocity greater than 20 cm/μs can be fabricated from a quasi-spherical wire-basket as illustrated in Fig. 1.   For this illustration the wall electrodes are at plus and minus 45 degrees latitude. Quasi-spherical loads require increasing mass density away from the equator due to the increasing magnetic field away from the equator where the driving current is closer to the axis of symmetry.
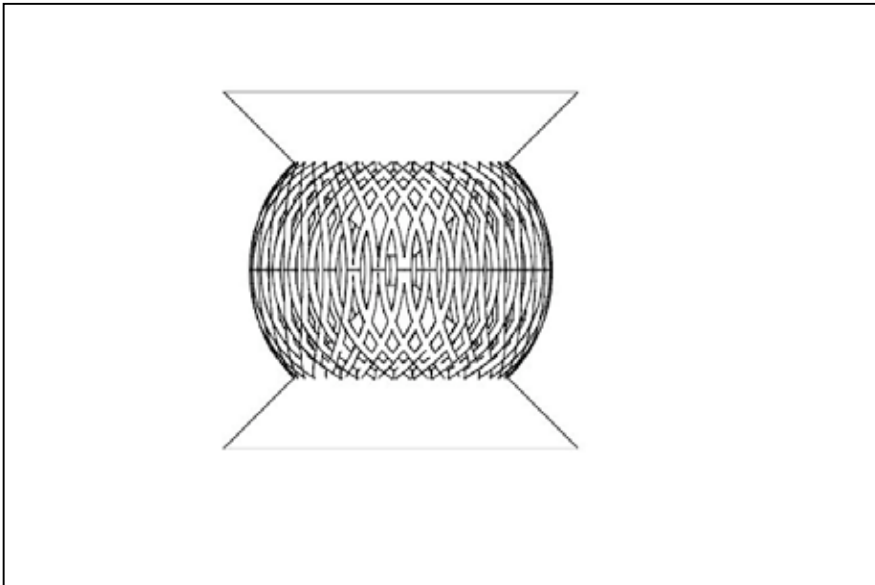
Fig. 1. Illustration of a quasi-spherical wire-basket with wall electrodes at plus and minus 45 degrees latitude

With the quasi-spherical wire basket the increasing mass density is realized by bending a wire element along a path as indicated in Fig. 2.   The typical first order quasi-spherical mass distribution gives the thickness of a complete shell increasing as the inverse square of the cosine of the latitude.   The equivalent mass distribution for a single wire is shown as the red curve in Fig. 2. [7] This curve has an exact analytical solution given by

$$\phi = \csc(\theta) - 1 \qquad (1)$$

Where

ϕ = Angle of longitude in radians

θ = Angle of latitude in radians
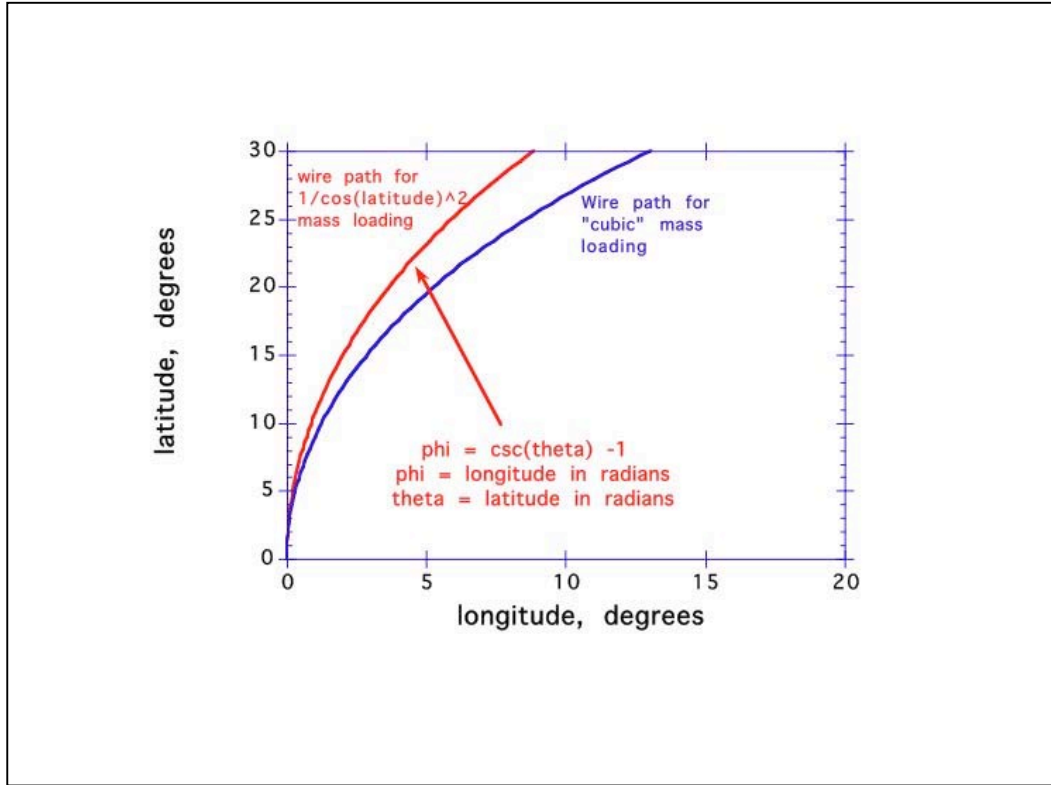
Fig. 2. The wire path for the standard quasi-spherical mass distribution has an analytical solution.   Wire paths that distribute more mass at higher latitude may be obtained from numerical integration.

Fig. 2 also shows in blue the wire path for a mass distribution than varies as the inverse cube of the cosine of the latitude.   Such a mass loading may be desirable to reduce mass running ahead at the wall electrodes.   The blue curve was obtained by numerically integrating the differential equation

$$d\phi/d\theta = (1/\cos(\theta))\sqrt{(1/\cos^{2(n-1)}(\theta) - 1} \qquad (2)$$

where n = exponent for power law mass distribution; n = 2 gives the typical quasi-spherical mass distribution with the exact wire path solution of equation (1).   Equation 2 may be numerically integrated to give the wire path for any value of n.
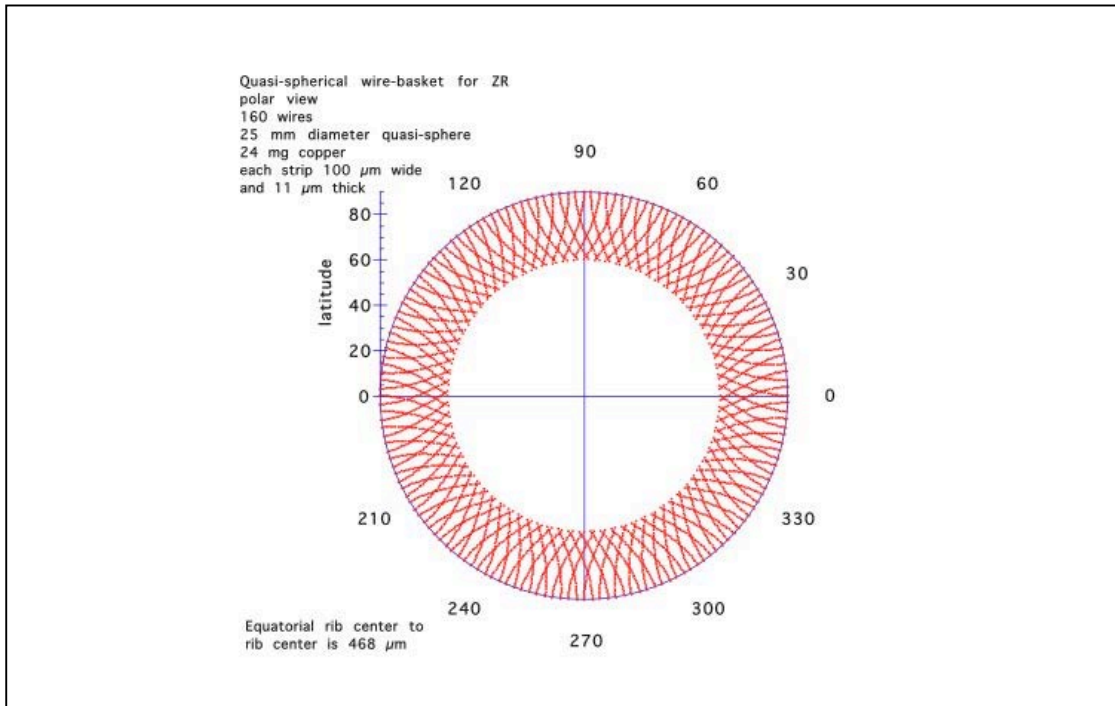
Fig. 3. Polar view of a wire-basket load for ZR at 25 mm diameter weighing 24 mg with wall electrodes at plus and minus 30 degrees latitude.

Fig. 3 shows a polar view of a wire-basket load design for ZR.   This load has wall electrodes at plus and minus 30 degrees latitude.   The wire paths shown are for the mass distribution varying as the inverse square of the cosine of the latitude.   This load is formed from 160 copper wire elements each with a cross sectional area of 1100 μm^2. The load has a 25 mm diameter and weighs 24 mg. We expect that the load can be fabricated by coating copper onto a mandrel, machining the wire pattern, and dissolving the mandrel.   Simulations of the implosion of this wire basket load show it reaching a velocity in excess of 20 cm/μs.   If the same load as shown in Fig. 3 were to be produced as a complete shell, it would be 2.5 μm thick at the equator and 3.25 μm thick at plus and minus 30 degrees latitude.   Such thin shells with a variable thickness with latitude would be very difficult to fabricate.
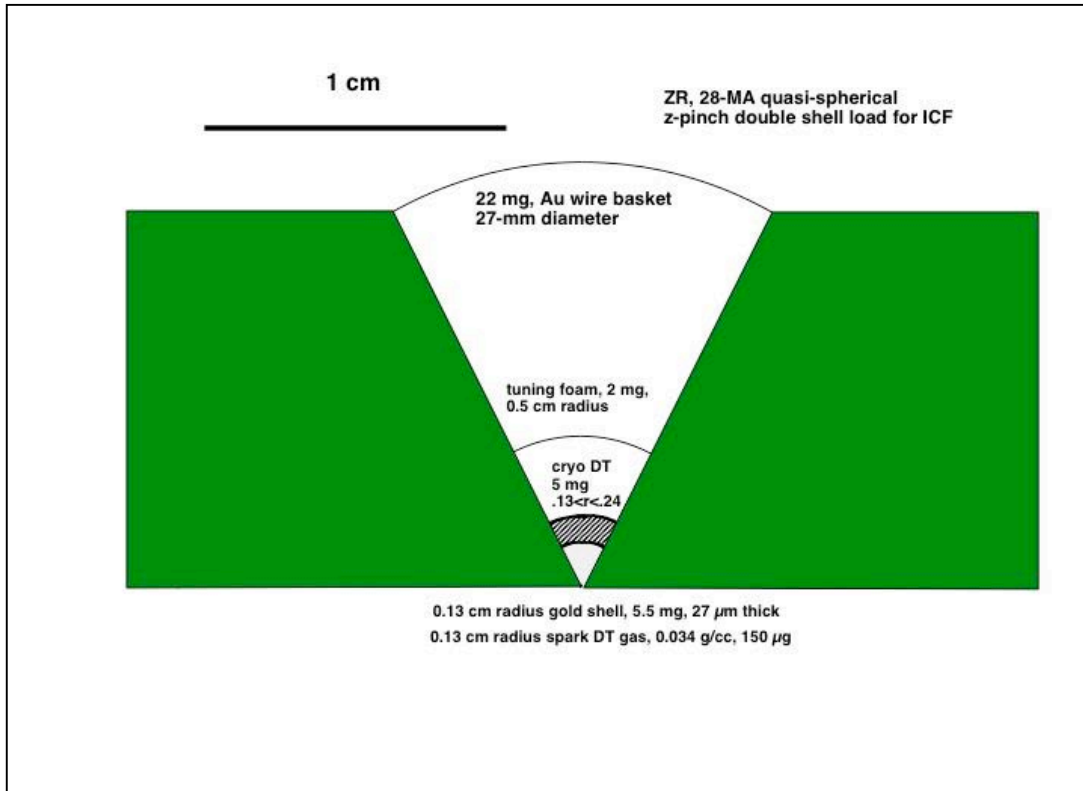
Fig. 4. A quasi-spherical double shell system for ZR.

Fig. 4 shows a double shell system for the 28 MA machine ZR with a 150 ns implosion time.   The 2D circuit source simulations of this load have a complete shell with mass density increasing with absolute value of latitude.   As such, the 2D simulations are approximations to the wire basket, which is in itself a three dimensional object.

These 2D simulations reveal that for single shell systems it is difficult to maintain the spherical shape of the implosion at the conical conductors.   For the initial 2D simulations reported here, the conical walls are treated as a perfectly reflecting boundary. Typically 2D simulations of single-shell systems show the shell near the cone running ahead of the rest of the shell, forming a bubble at the conical conductors. This bubble ultimately compresses internal DT gas into a pancake at the equator, limiting convergence to values too low for ignition.   If the DT is fielded as on-axis cryogenic fuel and driven by a larger diameter single shell, the cryogenic DT itself conducts current and deforms into a pancake well before the single shell implodes onto the cryogenic fuel.

In Fig. 4, we show a target with a layer of tuning foam at 6 mm radius with its mass increasing with the absolute value of the latitude. This added mass near the walls serves to stop the growth of the bubble at the inside of the outer shell where it intersects the wall. The mass of the main fuel in Fig. 4 also serves to slow the growth of shell instability.

Fig. 4 is a double shell system designed with the intention of the outer shell compressing a low Z material (DT in Fig. 4) which then implodes the inner gold shell filled with DT. The internal gold shell serves to trap Bremsstrahlung radiation from the inner DT fuel and thereby lower the ignition temperature to approximately 2 keV. A 2D simulation of the ZR load of Fig. 4 produced volumetric ignition of the inner shell DT and a yield of 12 MJ. However there is no margin for either ignition temperature or ignition density-radius product in this simulation of a ZR double shell and the zoning was too course to resolve the fastest growing, undamped modes of the Rayleigh-Taylor instability—modes with wavelength comparable to the scale length of the mass gradient.
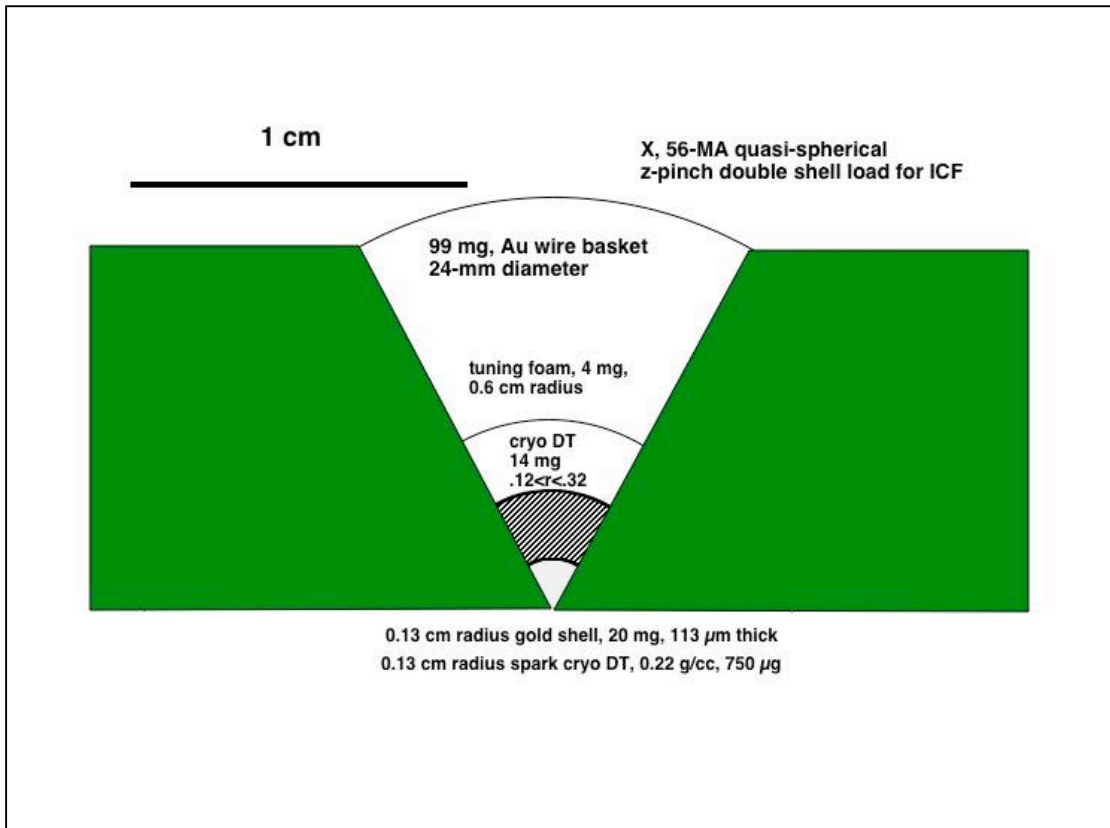
Fig. 5. A quasi-spherical double shell system for a 56-MA, 150 ns driver.

For the double shell load of Fig. 5, a double shell system driven by a 56 MA in 150 ns, there is considerable margin for ignition. This load gave an inner shell yield of 132 MJ, and a main fuel yield of 18 MJ. The load consists of a 99 mg gold wire basket at a 12 mm radius, a 4 mg tuning foam at 6 mm radius, and a layer of cryogenic DT which generates sufficient pressure to drive a 20 mg inner gold shell at a 1.3 mm radius filled with cryogenic DT.
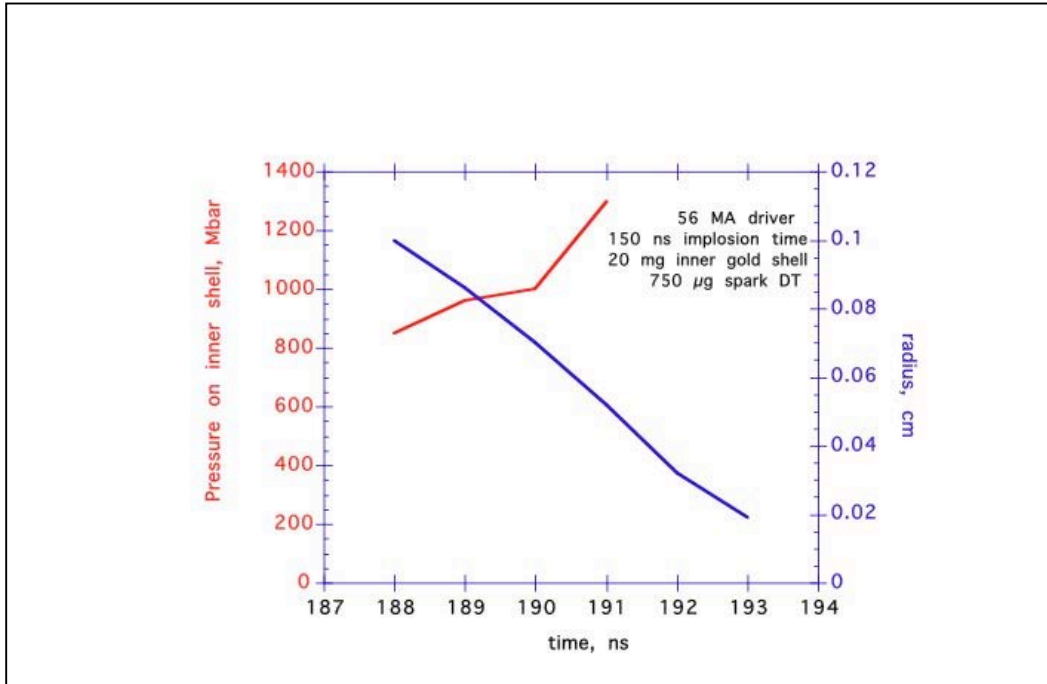
Fig. 6. Simulated inner shell drive pressure and inner radius versus time for the double shell system of Fig. 5

Fig. 6 plots the inner shell drive pressure and radius versus time for the load of Fig. 5. The drive pressure is approximately 1 Gbar and the inner shell velocity is 20 cm/μs.

Fig. 7 shows the inner shell fuel density-radius product reaching 1.5 g/cm^2 and the inner shell temperature reaching 2 keV just before ignition. The high inner shell fuel density-radius product leads to a large burn fraction of 58% in this 2D simulation.

However as shown in Fig. 8 the density-radius product of the main fuel in this load only reaches 0.33 g/cm^2. In order to ignite the main fuel, the density-radius product must reach 0.6 g/cm^2, more than the 0.3g/cm^2 requirement on the inner shell fuel, because main fuel would be ignited by an explosion of the inner shell, and the explosion lowers the density-radius product of the main fuel. The 2D simulation of the load of Fig. 5 shows the main fuel temperature reaching 4.4 keV due to the ignition and explosion of the inner shell, barely reaching the main fuel ignition temperature, because the optical depth of the outer gold shell is not enough to lower the ignition temperature by Bremsstrahlung trapping.
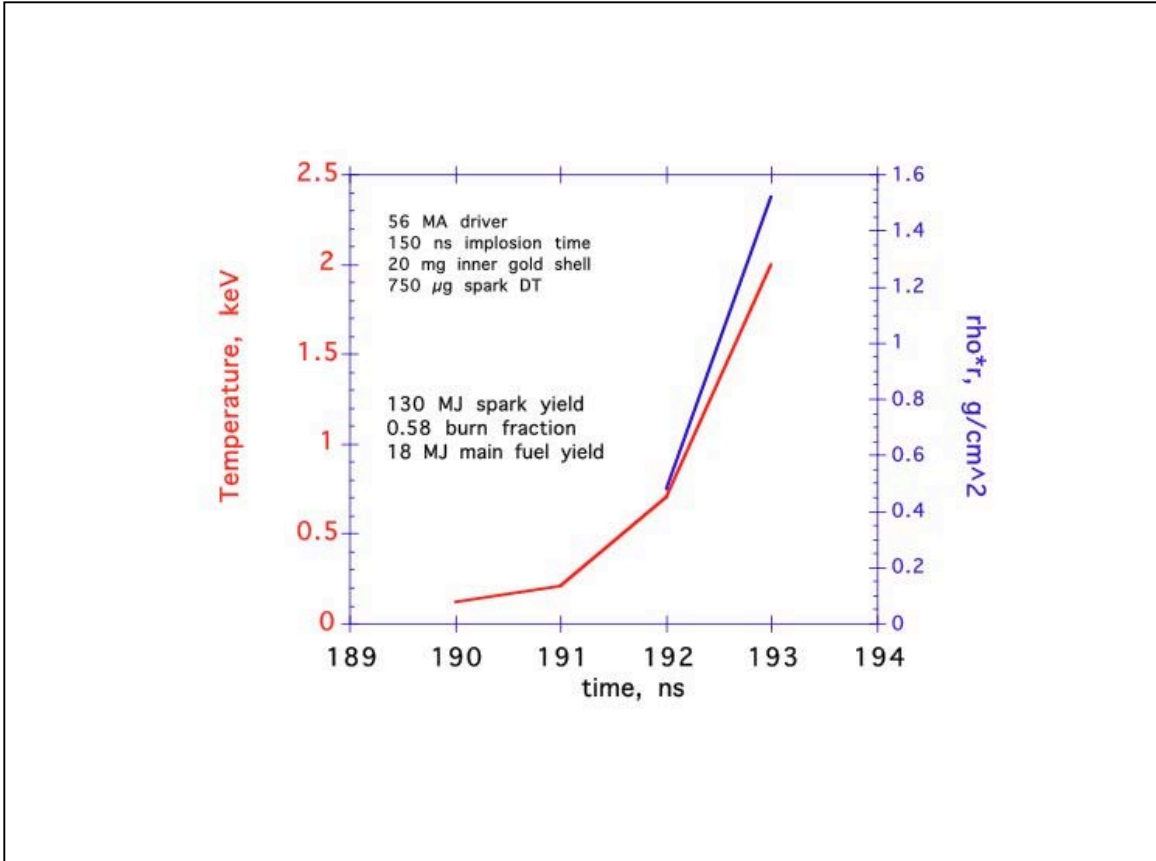
Fig. 7. Simulated inner shell fuel temperature and density-radius product versus time for the double shell system of Fig. 5.

Another advantage of the double shell system for achieving volumetric ignition is that the inner shell fuel can ignite in local thermodynamic equilibrium (LTE). As the inner shell fuel of Fig. 5 is compressed, its ion, electron, and radiation temperatures remain in equilibrium up to the ignition temperature of 2 keV. Since the primary effect of mix before burn is to equilibrate particle and radiation temperature, the inner shell fuel shows some resistance to the effect of mix preventing burn. Since the inner shell fuel of Fig. 5 is always in LTE during compression, mix will not reduce the ion temperature as the fuel is being heated to fusion temperatures.
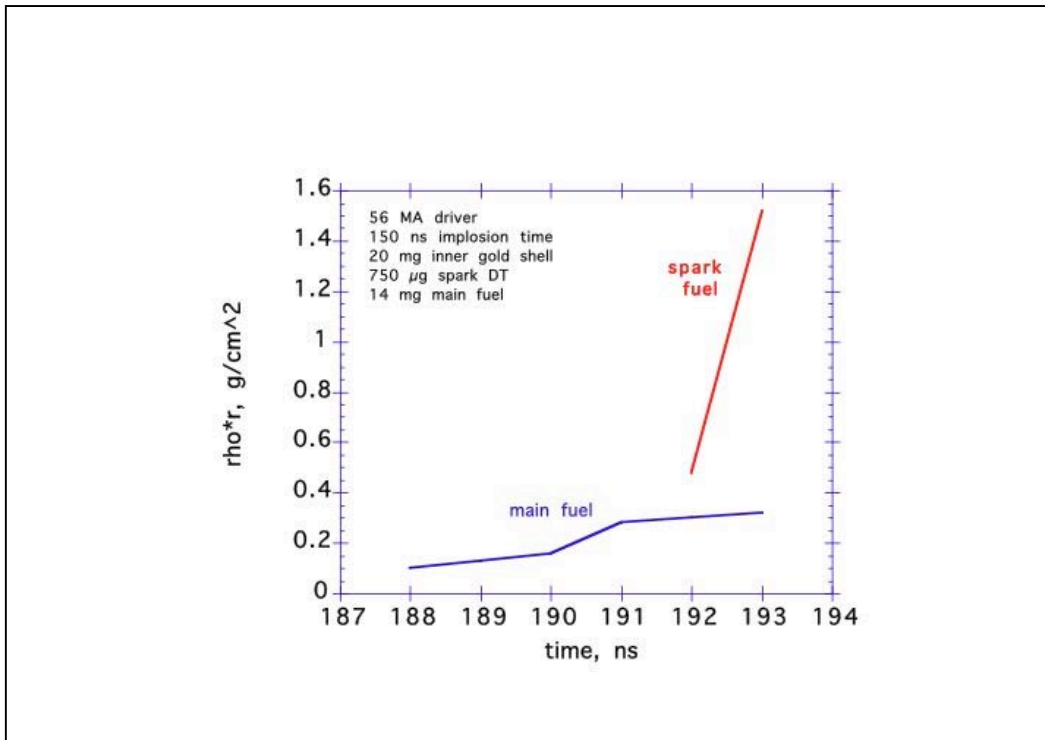
Fig. 8. Simulated outer shell fuel density-radius produce and inner shell fuel density-radius product versus time for the double shell system of Fig. 5. The outer shell fuel density-radius product is too low to ignite.

However mix in the inner shell fuel will have the effect of reducing the inner shell yield as shown in Fig. 9. Fig. 9 plots the peak burn ion, electron, and radiation temperature, and yield, versus mass fraction of gold impurity in the inner shell fuel. At a mass fraction of 4% gold, the peak burn temperatures have equilibrated at 8 keV and fall to 6 keV at a mass fraction of 14% gold. The yield drops from 115 MJ at 0% mass fraction to 17 MJ at 4% mass fraction to less than 10 MJ at 14% mass fraction.

The loss of yield due to mix in the inner shell will also make it difficult to burn the main fuel. If we include mix in the main fuel, the main fuel would have to be heated to more than 4.4 keV to burn efficiently.

We conclude that burning the main fuel in the outer shell of a double shell system like that of Fig. 5 is not practical.
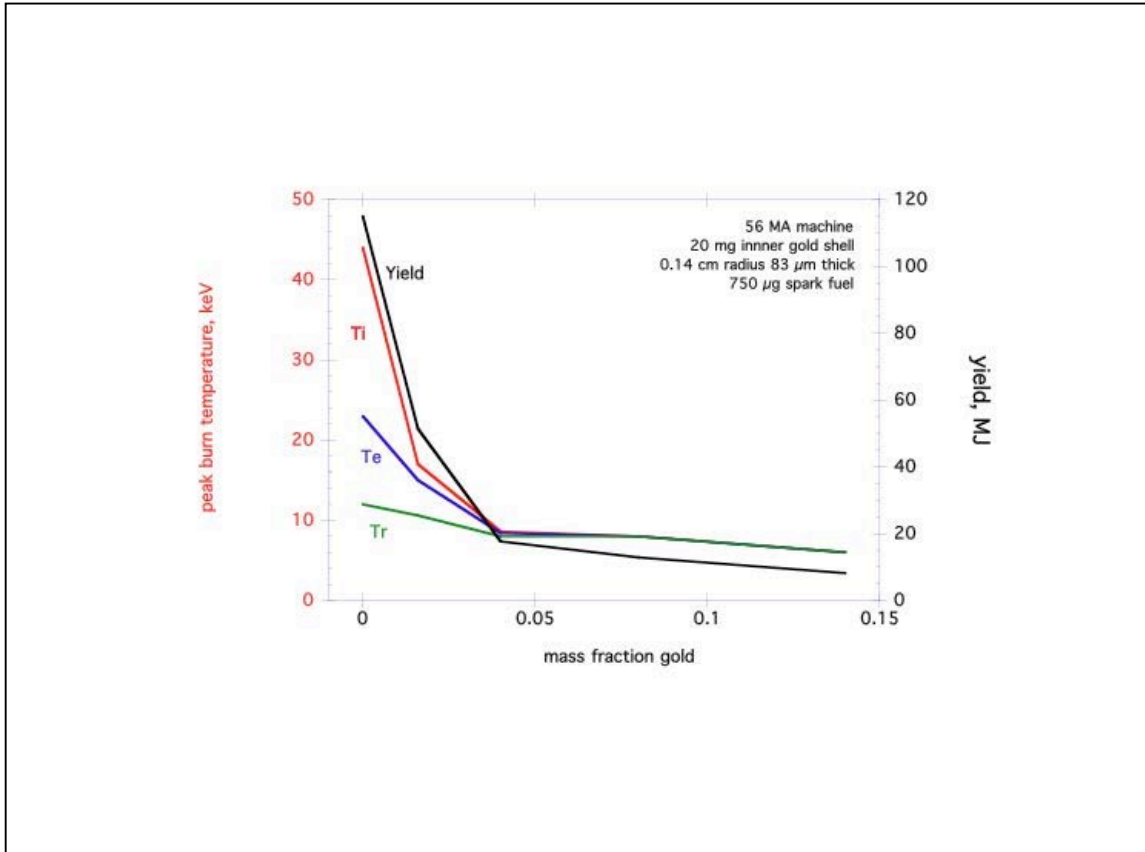
Fig. 9. Simulated yield and inner shell peak fuel temperatures versus dopant mass fraction of gold in inner shell fuel. The dopant simulates the effects of complete mix. To increase ignition temperature margin the initial inner shell diameter is slightly larger than the inner shell diameter of Fig. 5. At a mass fraction of 4% the inner fuel burns at an LTE temperature of 8 keV and the yield is lowered a factor of 8 with respect to 0% mass fraction.

One way to improve upon the 132 MJ inner shell yield from the load of Fig. 5 is to speed up the pulsed power to less than 100 ns implosions, and drive single shell systems. These single shell systems would be at smaller diameters than the 150 ns implosion systems and could be fabricated as complete shells rather than wire baskets. The single shell systems may be stable due to the faster implosion times and lower in-flight aspect ratios and for the same machine current the single shell systems can heat roughly 4 times the DT mass in the inner shell of a double shell system. The results of simulations with single shell systems will be given in section IV on QSDD2.

III. Magnetically Insulated Current Amplifier (MICA)

The baseline configuration of ZR is suitable for driving experiments on the isentropic compression of materials, high-energy density physics, inertial confinement fusion with x-rays, and double-shell quasi-spherical direct drive (QSDD1) capsules with a wire-basket plasma. [7] However, the baseline pulse has too slow a rise time for driving quasi-spherical direct drive (QSDD2) capsules, which are single-shell capsules directly driven by the magnetic pressure from current flowing through the pusher. [9] In addition, X-ray production with z-pinches and QSDD1 capsules could both benefit from a shorter duration and higher current pulses than ZR can provide in the baseline configuration. [10]

In fact, the scaling relations developed in Reference 10 for z-pinch driven, thermonuclear-fusion experiments show that the pinch current and accelerator power required to achieve a given value of x-ray power are proportional to the implosion time, the required accelerator energy is proportional to the square of the implosion time, and the efficiency of the system (expressed as the ratio of the x-ray power to the accelerator power) scales inversely with the implosion time. Since the cost of such a driver scales with the accelerator power and energy, finding a way to reduce the implosion time substantially and efficiently has considerable value.

The electrical breakdown of the vacuum insulator is the major impediment to producing shorter pulses. The bottleneck of the vacuum insulator inductance can, in principle, be mitigated by 1) storing the energy in an azimuthally propagating wave in multiple, parallel, inwardly spiraling, self Magnetically Insulated Transmission Lines (MITLs), 2) extracting the energy with multiple parallel switches on the top edge of each MITL, and 3) feeding energy into a radially converging convolution to a central load.   Since the effective impedance of the wave propagating in the axial direction is much less than the wave impedance propagating in the azimuthal direction, the switching increases the current potentially available to the load. Modest pulse shaping for QSDD2 can be obtained by 1) letting the main pulse feed the central load for a first pulse, 2) switching additional energy from the MITLs, and 3) varying the switch timing to fine tune the shape of the main pulse. Destructive and constructive interference of the waves in the MITLs, the inductance of the switches and convolutions, and the potential for breakdown of magnetic insulation determine the potential efficiency of the device.

The concept of charging a line in one direction and discharging it in an orthogonal direction was proposed by retired Sandian and Erwin Marx Award Recipient T. H. Martin in the 1970s. The concept used liquid dielectrics and was called sidewinder. The current proposal is a self-magnetically insulated version of the liquid-dielectric sidewinder.   To our knowledge, Tom was also the first to suggest that self-magnetically insulated transmission lines might store electromagnetic energy that could be switched into a load for an additional pulse compression stage in vacuum. We asked Tom if he had pursued the idea and he replied that he had not because the need for very short pulses was obviated by the move to ion beams for fusion.   The device proposed in this paper revives Tom's suggestion. It is called a Magnetically Insulated Current Amplifier (MICA). The equivalent circuit is shown in Fig. 10.
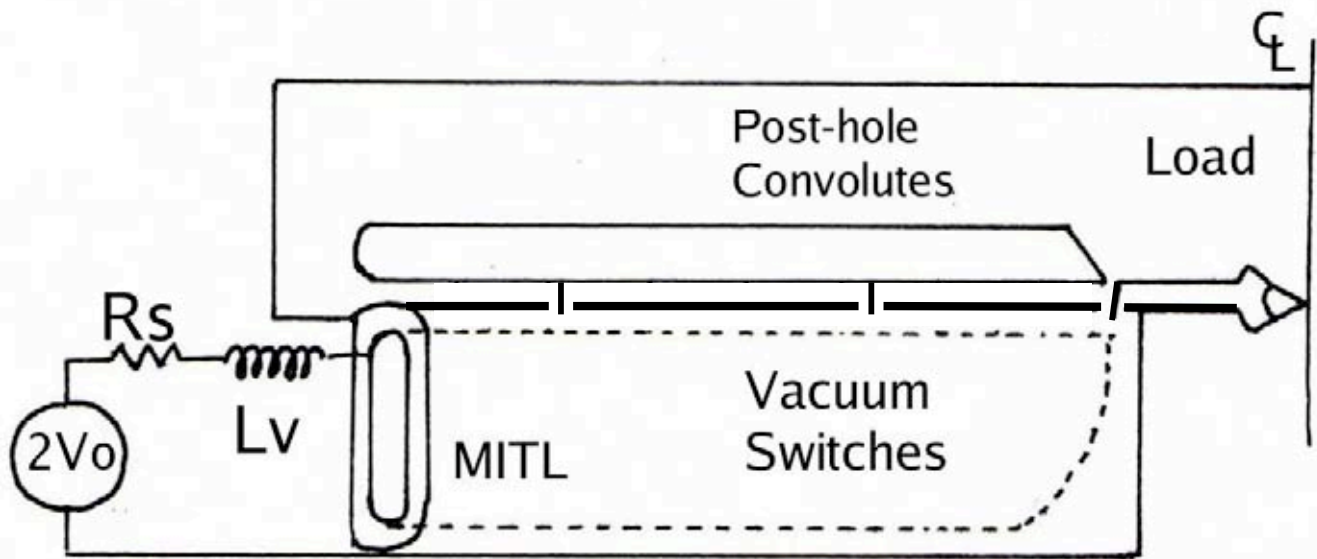
Fig. 10: Circuit Schematic of MICA

The MITL is shown as a distributed circuit element. The Poynting vector flows from left to right to charge the MITL and provide an optional pulse-shaping step in the current to the load through the right most post-hole convolute. The switches on the top then break down simultaneously and the MITL discharges into the top MICA Power Feed (MICA_PF).

The addition of another stage of pulse compression on ZR should decrease the overall jitter—if the switching works—to improve precision and increase the output current to increase performance. The convoluted path from the load to the vacuum insulator should allow multiple shots between maintenance to increase Z's post-refurbishment capacity.

The design has progressed through seven versisons during this project. Version 5 is the baseline and in shown in Fig. 11. Versions 6 and 7 have modifications to improve the maintainability and flexibility and are briefly described in the discussion but have not yet been incorporated into the baseline configuration.

The MICA is designed to be an alternate MITL for ZR and mates to the baseline ZR vacuum stack through the five MITL support rings. An exploded view of the assembled module is shown in Fig. 11 and then each element is explained in the subsequent paragraphs.

MICA Power Feeds

(Replaced by simpler, more maintainable, more versatile, and less expensive triplate design for version 6 and 7)

Ground Plane with Switch Holes

Spiral MITL

Mating rings between vacuum insulator stack and spiral MITLs
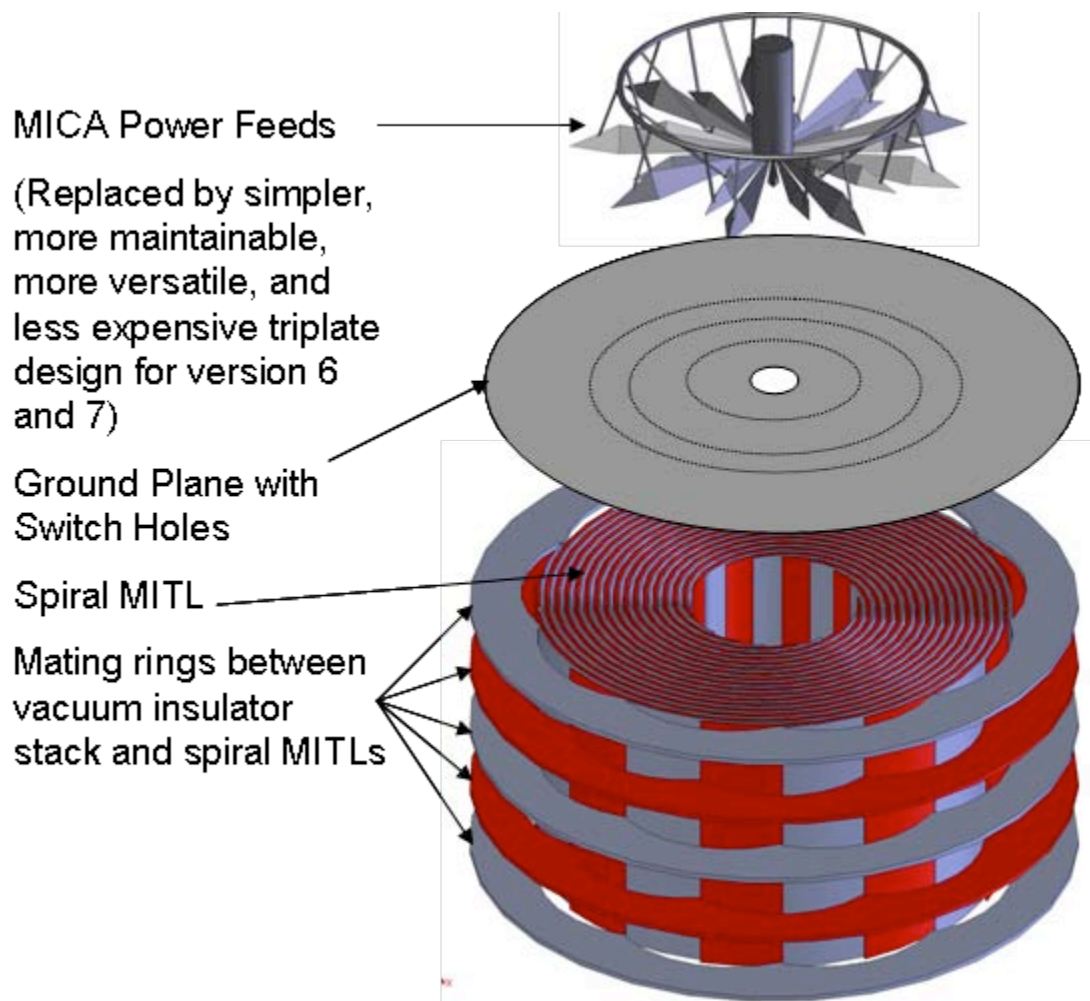
Fig. 11: Exploded View of MICA.
Bottom: Mating rings between vacuum insulator stack and spiral transmission lines,
Middle: Top ground plan covering the spirals, and
Top: 27 MICA Power Feeds (MICA_PFs) with high voltage inductive supports to the central load for version 5.
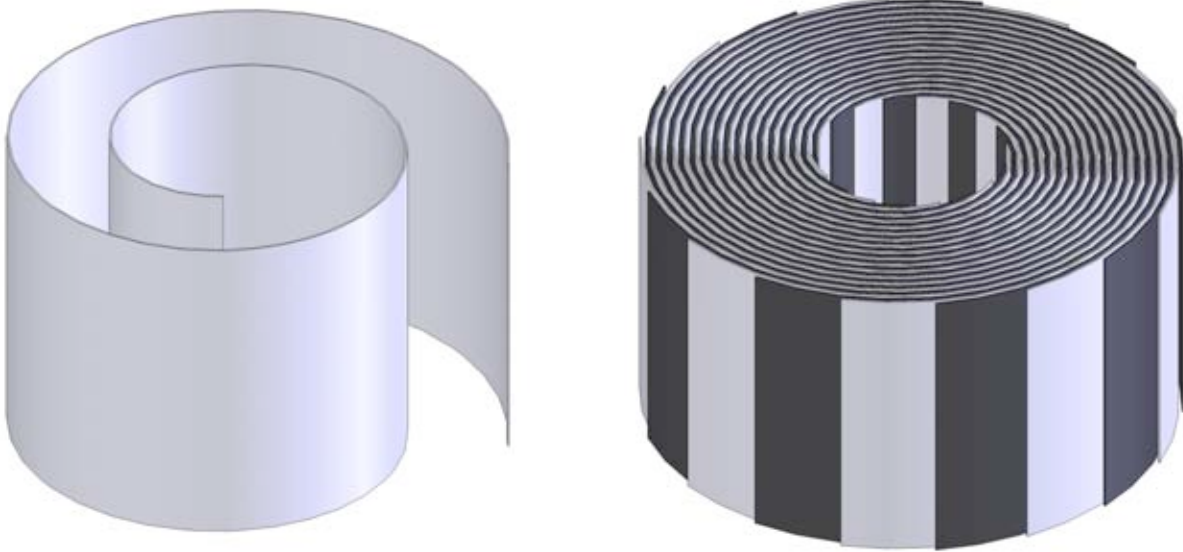
Fig. 12: Left: View of one of 18 MITL conductors (9 ground spiral conductors interleaved with 9 high voltage conductors) shown spiraling towards the center. Right: View of assembled MICA Storage Section

The pulse storage section consists of 9 nested vertical triplate MITLs with shared ground conductors. The ensemble spirals azimuthally around a central ground conductor, which gives diagnostic access to the load, and fills the available volume. The power flows into the load through 3 sets of 9 switches penetrating the ground plane in post-hole convolutes on top of each of the 9 modules to a set of 27 MITLs in the MICA_PF and then through a common radial-disk transmission line to the load.

Design Constraints of Spiral Lines

The variables are defined as follows with all units in the mks system:
V= MITL voltage
d_o = vacuum gap at the input to a MITL
Δ = conductor thickness
c = speed of light in vacuum = 3×10^8 m/s
u = wave velocity of the self-magnetically insulated front ~0.7c for V> 1 MV [11, 12] and reflects the erosion of the front, which is very severe for V< 1MV and provides a useful pulse shaping feature
t_1 = pulse duration into the MICA
t_2 = pulse duration of the foot, if any
t_3 = pulse duration of the main pulse out
N = number of MITLs in parallel in the vacuum
Z_o = vacuum wave impedance of the N MITLs in parallel

Z = operating impedance of all N MITLs in parallel

Z= 0.75 Z_o for a MITL operating in the self limited mode at V > 3MV as shown in [12]

L = physical length of each MITL

h = height of each MITL conductor

w = width of each MITL

H = height of the vacuum cylinder containing the MICA, not counting the space for the top disk feed.

R = radius of the vacuum cylinder containing the MICA, not counting the vacuum stack transition.

V_V = volume of vacuum available for MICA = $\pi R^2 H$

Tapering the line to give a reflected wave that should pull the electron cloud closer to the cathode and aid magnetic insulation can be used if it is necessary to improve insulation.

Since the adjacent MITLs share a ground plane, the width w of each triplate MITL is
$$w = 2(d_o+\Delta). \qquad (3)$$
The Length of the MITLs is just long enough to absorb a pulse of duration t_1 less the foot of duration t_2 less the duration of the main output pulse t_3. Therefore,
$$L = u(t_1 - t_2 - t_3) \qquad (4)$$
but is then optimized with simulations for best coupling to the load.

The height of each line is determined by the desired MITL impedance:
$$h= 377\, d_o/(2NZ_o) =0.75* 377\, d_o/(2NZ_o)=141 d_o/(NZ) \qquad (5)$$
The total volume V_T of the N lines with shared ground conductors is calculated as N times the volume of 1 line with gap d_o.

Therefore, $V_T= NLhw$. Obviously, $V_T < V_V$, so the selection of parameters should allow for N=9 lines in parallel with H< 2.0m (the full height of the vacuum insulator) and R = 1.34 m to allow the transition from the vacuum insulators to the input to the MICAs . The parameters for the baseline case for the ZR MICA were determined by iterating the mechanical and electrical designs to produce a high performance design that can be manufactured. The parameters are shown in the following table.

Parameter	Value
Zmitl/Zo	0.75
V	4.50E+06
Z	0.179
beta	0.7
t1	1.00E-07
t2	2.00E-08
t3	1.50E-08
c	3.00E+08
DELTA	1.00E-02
max del	6.50E-01
del	2.50E-01
d	1.75E-02
MICA Height for 9 lines	1.535730912
L	1.00E+01
MICA Volume	7.60E+00
MICA Radius	1.34
Vacuum Volume	8.663117977
Fraction Used	8.77E-01
Radius for 90%	1.32E+00

Table 1: Baseline parameters for ZR MICA

MICA Power Feed (MICA_PF) Baseline (Version 5)

The MICA_PF consists of a top ground plane with 27 tapered channels of triangular (equilateral) cross section mating to a lower ground plane with the holes for the 27 switches. The 27 high voltage lines are in 3 sets of nine lines called MICA1 (beginning at r= 1.22 m), MICA2 (beginning at r= 0.92m), and MICA3 (beginning at r= 0.47 m). The disk feed operates at high voltage and is inductively isolated from ground.
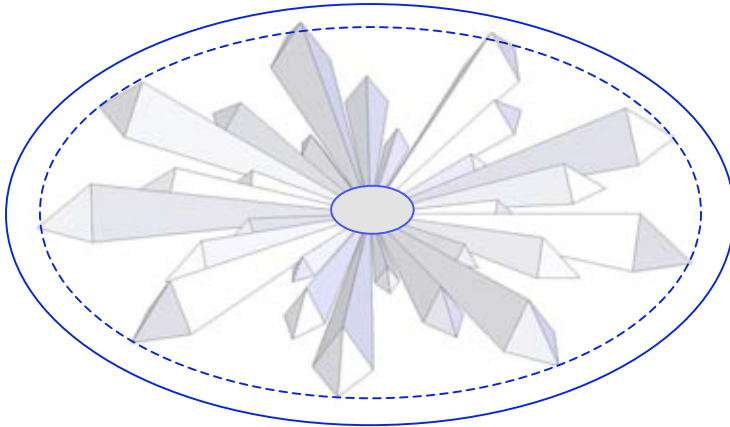
Fig. 13. View of high voltage lines in top convolute. The 27 switches, in 3 sets of 9 each, are located at the outermost points of the MICA lines.

The design study examined 1 mm to 3 mm vacuum gaps in the MICA power feeds. The smaller gaps gave more current to the load but had more electron losses and greater problems with mechanical tolerance. The baseline (Version 5) design is compatible with an adjustable gap by raising or lowering the top ground conductors and high voltage conductors of the MICA_PFs with respect to the ground plane.

The multi-tri-plate design that replaced the one shown in Fig. 13 for versions 6 and later can easily and cost-effectively change the Zflow losses by changing the height of the tri-plate high-voltage conductors and adjust the vacuum gap by adjusting the final alignment. The tri-late gap separation is 3 mm and operates as a self-magnetically insulated transmission line with 45 deg tapered lines mating each line to its switch and to the disk feed.

The best performance for precision, shot capacity, and performance are achieved by trading off low inductance for low electron flow.

SCREAMER simulations with the Version 5 Power Feed shown in Fig. 11-13 showed that electron losses in the Power Feed limited the current to the QSDD2 load. These losses might cause additional losses if they were to turn on ion emission from the anode. Therefore, the design was modified to give two options for Version 7: 1) a minimum vacuum wave impedance of 1.0 Ohms for each set of 9 Power Feeds for capsules that do not require precise pulse shaping and for wire arrays and 2) a minimum vacuum wave impedance of 0.6 Ohms for each set of 9 Power Feeds for driving low-adiabat capsules with pulse shaping.

Critical Physics Issues

The critical physics issues related to the feasibility of the MICA are the effective load line, the interference of waves in the MICA Spiral MITLs, electron (Zflow) losses, and MITL gap closure.

MICA Load Line

One-dimensional SCREAMER simulations and three-dimensional Quicksilver simulations were performed to determine the MICA Load Line—the voltage out of the MICA switch and into a resistive load as a function of the current through the switch. The SCREAMER model was used to calculate the voltage and current into a resistive load impedance from the vacuum wave impedance of the 9 parallel, MICA spiral MITLs with a combined vacuum wave impedance of 0.239 Ohms. The results are compared with the load line of the spiral self-limited MITL based on the MITE experiments. [13]

MICA and Self-Limited MITL Load Lines
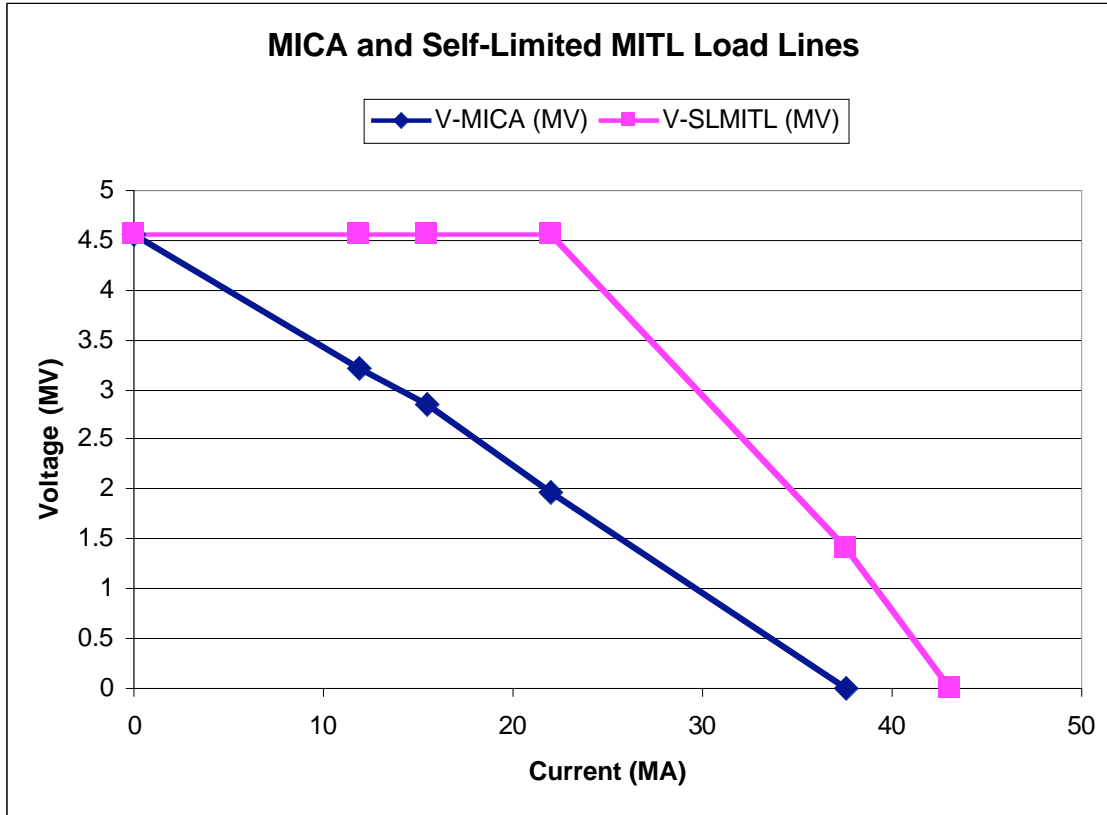
Fig. 14: The results for the MICA Load Line are shown with the self-limited MITL Load Line for ZR.

Each MICA produces lower peak power than ZR would produce into a single load—but several MICAs can be added in parallel with the output at the end of the spiral MITLs to provide more current into the common load. The MICA load line has the form of a conventional (non-MITL) load line of impedance equal to the open circuit voltage

divided by the short circuit current. The SCREAMER simulations predict a matched source impedance Z_{MICA} of the MICA_PF is (4.5MV)/(37.6MA)= 0.119 Ohms = 0.50 Z_o for MITL vacuum wave impedance Z_o. However, this result is sensitive to the approximations of the SCREAMER MITL model.

Therefore, we did a self-consistent, three dimensional, Quicksilver simulation of a simplified MICA_PF. The anode-cathode gaps were unchanged at 1.75 cm separation of the anode and cathode plates and 2.0 cm on top at the switch. The overall length and height of the MICA were scaled down by a factor of 10 to 1.08 m length and 0.2 m height. Further computational savings were made using the symmetry of the simplified structure. The load impedances for each of the two switches shown in Fig. 15 are varied to find the load line shown in Fig. 16.
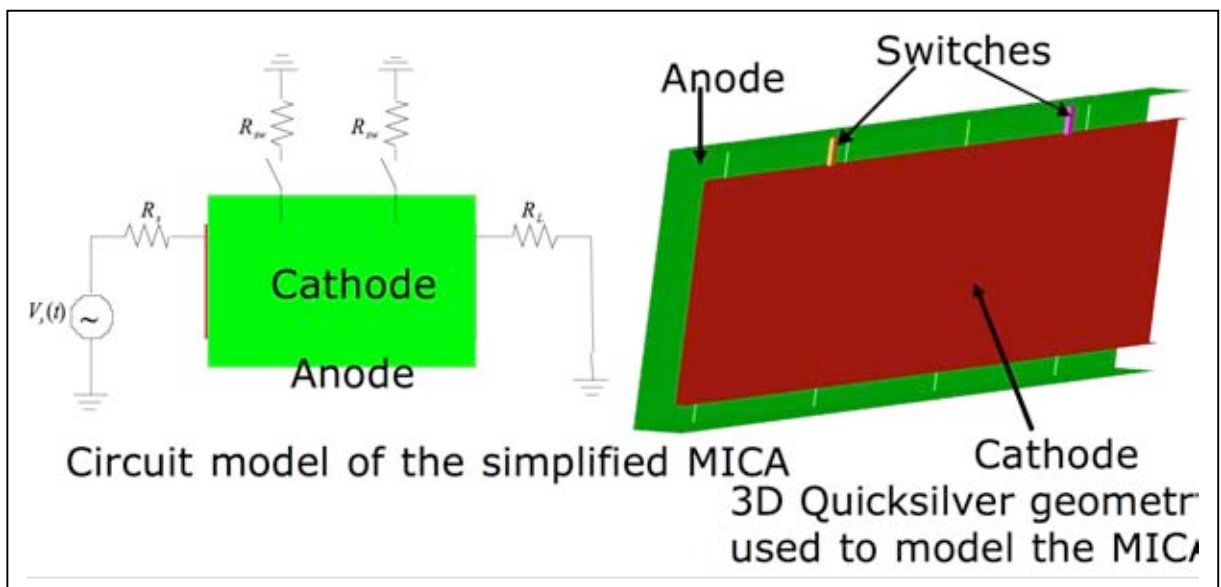
Fig. 15: Schematic for QUICKSILVER 3-D Simulations

MICA Load Line

$Z_o = 17.58\ \text{Ohms}$
$Z_{SL} = 11.34\ \text{Ohms}$
$I\,(ZM=0) = 0.335\ \text{MA}$
$I_{matched} = 0.1675\ \text{MA at}$
$V = 1.9\ \text{MV}$
$Z_{MICA} = 11.34\ \text{Ohms}$
$Z_{MICA}/Z_o = 0.64$
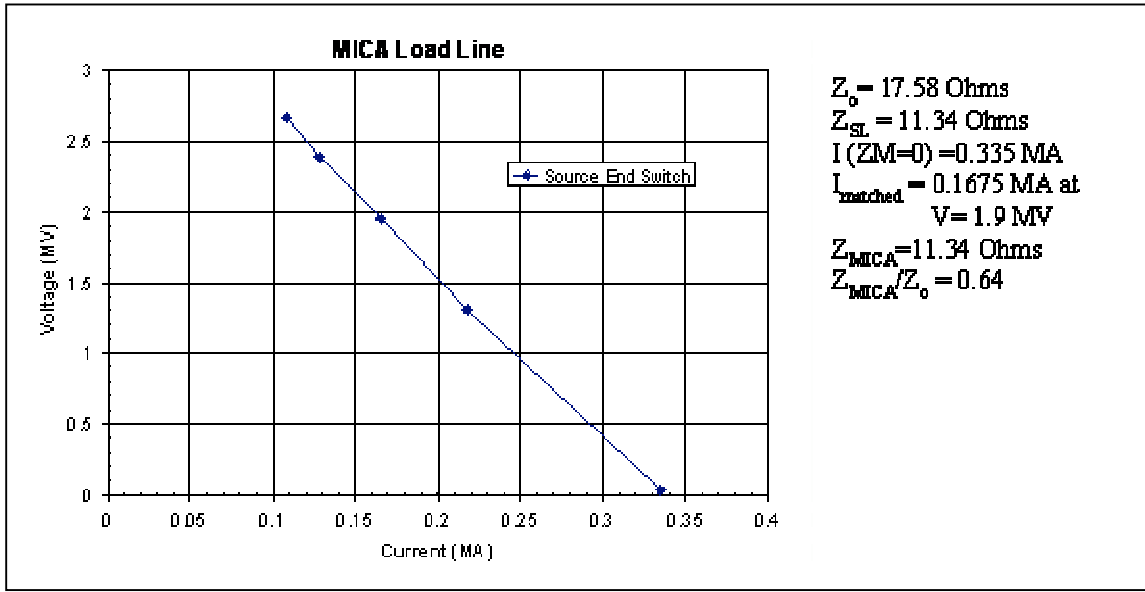
Fig. 16: MICA_PF Load Line

In contrast to the SCREAMER results of $Z_{MICA} = 0.5\ Z_o$, the Quicksilver simulations show the $Z_{MICA} = 0.64\ Z_o$, which equals 0.154 Ohms for ZR.   We will use the higher-fidelity value of $0.64\ Z_o$ from Quicksilver.

Interference of waves in the MICA Spiral MITLs

The same Quicksilver simulations provided insight into the effects of wavefront interference in the MICA's spiral MITLs. As shown in Fig. 17, the electron dynamics at the intersection of the wavefront from the two switches were benign. The voltage falls upon switching faster than the current falls, so efficient magnetic insulation is maintained.
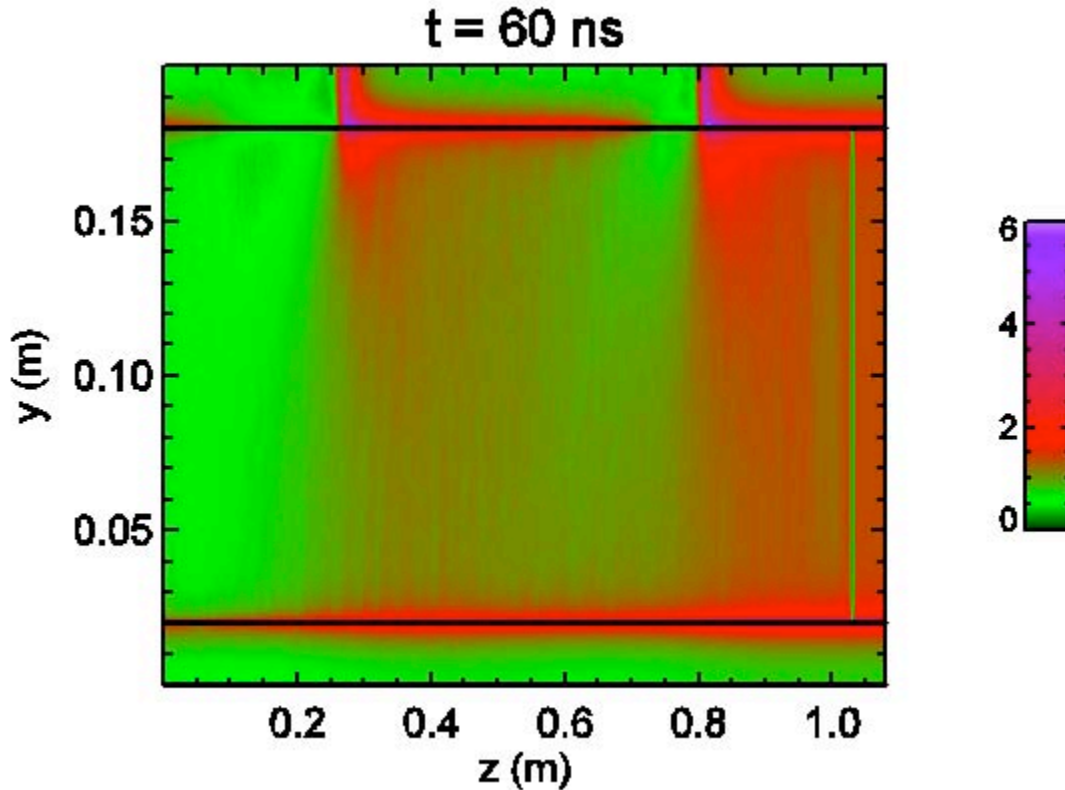
Fig. 17: Qualitative view of the magnetic distribution after switching. The wave is injected from the right and the load is on the left. Red indicates high magnetic field and shows a benign progression without any destructive interference through both the MICA switches. The scale is in Tesla.

Z_{flow} Losses

Electron losses associated with the transitions in geometry of magnetically insulated transmission lines have been examined theoretically by C. W. Mendel et al [14] as an impedance $Z_{flow} = V/(I_T^2 - I_B^2)^{0.5}$, in which V= Voltage, I_T = the total current before the transition, and I_B = the boundary current flowing in the cathode. The model assumes that most or all of the electron flow current is lost before it reaches the load. Experiments on Z indicate that $Z_{flow} = 0.25$ Ohms describes the losses in the Z convolute. However, the MICA convolute is a much more gradual transition than that used in Z. The closest experiment to the MICA parameters was the MITE experiment with the tapered transmission line to a diode load. [13]

The tapered-line convolution on MITE connected $Z_o = 7.6$ Ohms to $Z_o = 20$ Ohms in 0.5 m. The efficiency of the current transport through the convolution as a function of the load impedance, normalized to the vacuum wave impedance before the convolution, is shown in the Fig. 18, adapted from Fig. 17 of reference 13.
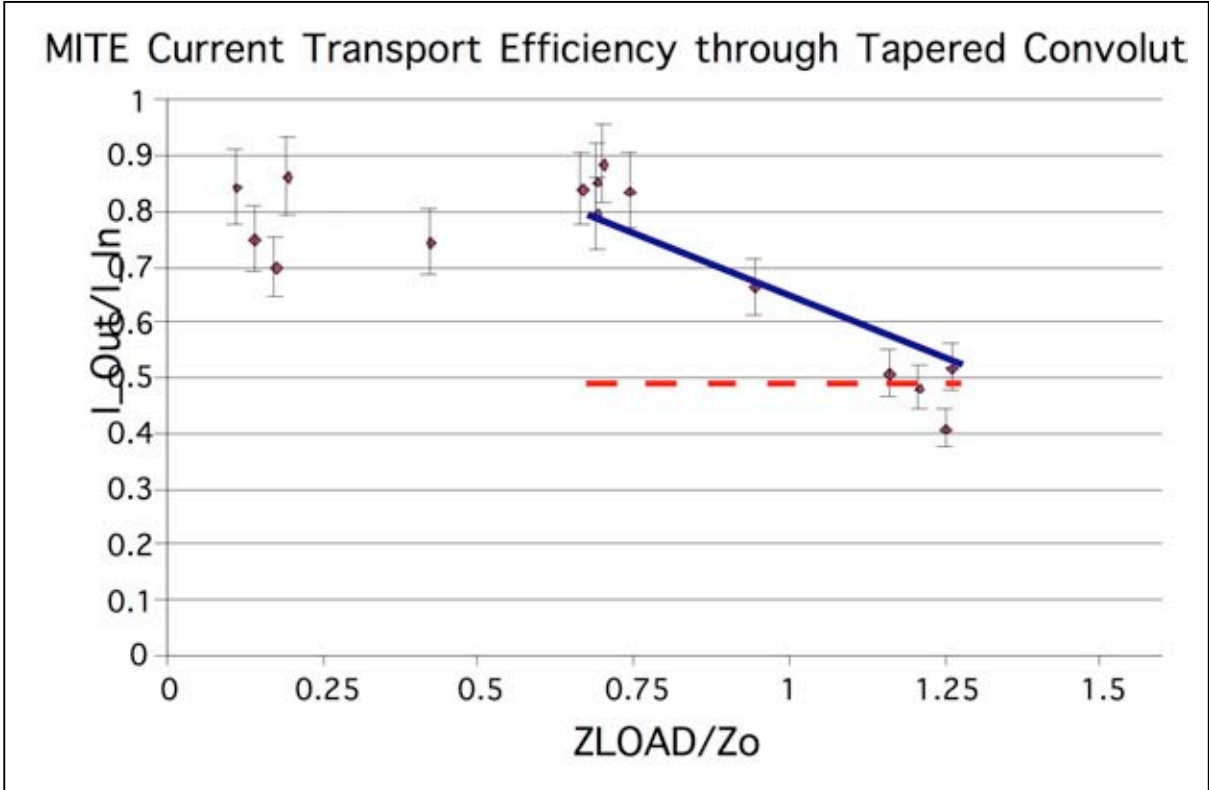
Fig. 18: Comparison of current transport efficiency through the MITE convolute with that predicted by two assumptions for Z_{flow}. The bars represent the 8% one-sigma standard deviation of the composite measurements. The blue line gives the best fit to the data for $Z_{flow}=0.79\ Z_0$ and the red line represents the assumption that all electrons in the flow are lost.

The measured efficiency is compared with 1) I_{Load} = the measured I_B and 2) $Z_{flow}=0.79$ $minZ_o$, in which $minZ_o$ is the minimum vacuum wave impedance of the power feed. The model with $Z_{flow}=0.79\ minZ_o$ provides the better fit to the data. Therefore, we will use $Z_{flow}=0.79\ Z_o$ to design MICA experiments and predict the performance of ZR_MICA.

<u>Gap Closure and Ion Losses</u>

The 1 mm spacing near the load is very desirable for useful performance of the MICA system on ZR—which is why high-performance self-magnetically insulated power flow is the most important enabling technology for MICA. If the gap closes at 2 cm/usec, the gap will close in ~50 ns, shortly after the implosion is completed. However, ion losses prior to the closure would preclude successful operation of the MICA. The limits will have to be determined by experiments--with the low x-ray emissions and < 50 ns implosion time characteristic of a MICA-driven capsule.

Such experiments should be designed with full consideration of currently available data, the most comprehensive and relevant of which are from Stygar, et al on Z. [15] The data consists of only 17 points for eight configurations--two current levels and four MITL gaps per current level. The experiment measured the load current, x-ray power, and x-ray energy for each configuration. For the 19 MA experiments, the x-ray energy and peak x-ray power with a 1mm gap is, respectively 60 % and 80% of that with a 3 mm gap. More generally, Fig.s 3 (peak x-ray power), 4 (total radiated energy), 5 (time resolved current and x-ray power for the 13 MA shots), and 6 (time resolved current and x-ray power for the 19 MA shots) of Reference 15, provide convincing and consistent evidence of gap closure for the 1 mm gap—but only after ~100ns of current flow and after the in x-ray power has reached its peak flux. In contrast the MICA approach for quasi-spherical direct-drive fusion requires only ~50 ns conduction time and the 30-eV temperature of the capsule produces orders of magnitude lower radiation flux than does a wire array— until after the thermonuclear fuel has ignited. Therefore, the data does not necessarily preclude 1 mm gaps working at higher currents in a low-x-ray environment for 40 ns implosion times.

However, the MICA peak linear current density is 18 MA/cm while the Z experiments in Reference 15 were carried out at only 3 MA/cm. Marcus Knudson has not observed any effects from gap closure with 7 MA/cm linear current densities (15 MA with effective width of 22 mm) and 0.75 mm vacuum gaps in Isentropic Compression Experiments with ~300 ns ramped pulse and a low-flux x-ray environment. [16]

Since the MICA pulse is much shorter than the pulse in both these experiments and the electron flow is even more tightly insulated on MICA, then we conclude that the 1mm gaps and 18 MA/cm linear current densities are not precluded by the available data. Experiments in the 18 MA/cm regime for an implosion time of 50 ns in a low-x-ray environment are needed to fully qualify the design for ZR-MICA.

Vacuum Switch

Fast vacuum insulated switches have not been developed. Four ideas for possible switches should be tested and there may be others.
   I. Use a metal or carbon coated switch electrode projecting from the anode.
   III. Use a carbon coated electrode projecting from the cathode to induce closure with a negative-ion-neutral ensemble (suggested by Rick Spielman in private communication.)
   IV. Use a plastic coated electrode projecting from the anode to induce closure from positive ion flow.
   V. Induce closure with a laser trigger to the cathode or anode.
The first two of these were briefly explored on the Tesla accelerator with very helpful consultations with Mark Savage at ~650 KV and ~270 KA to look at the feasibility of using the simplest possible switch--a metal rod extending across a portion of the MITL gap. The gap between the cathode and the switch electrode was varied from 0 to 5 mm. A bare brass electrode and a carbon coated electrode were tested. Fig. 19 shows the experimental arrangement and Fig. 20 shows a typical set of voltage and current waveforms.
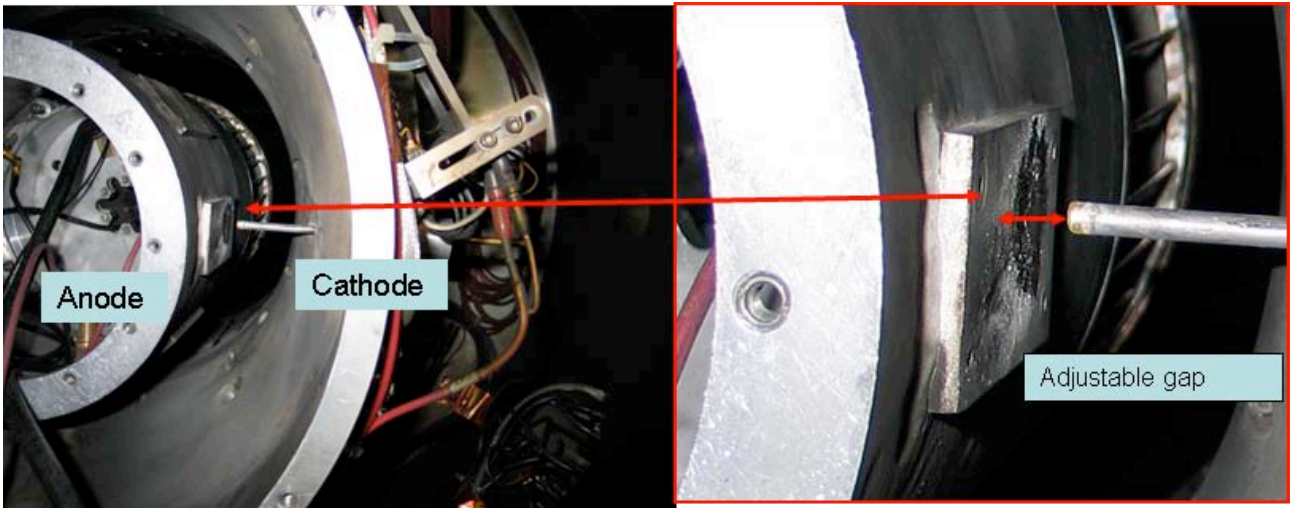
Fig. 19: Layout of Tesla Switch Experiment
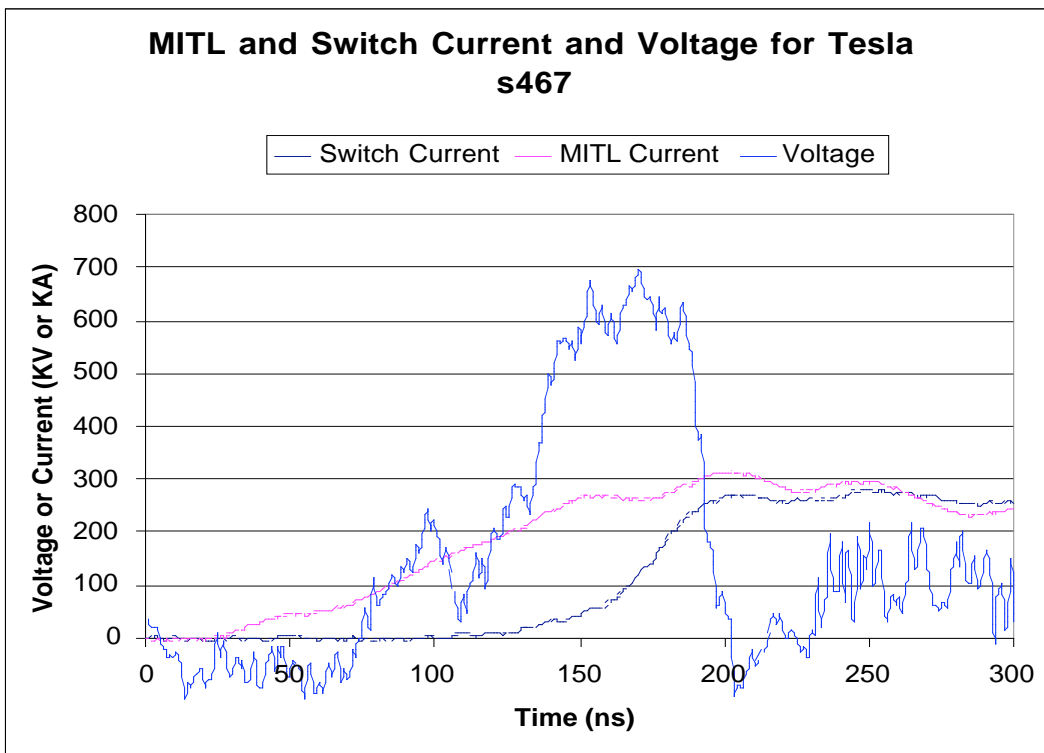
Fig. 20: Voltage and current waveforms for Tesla Switch Shot s467.

The five shots with non-zero gap that shorted during the pulse were analyzed for the e-folding time of the resistance fall. The results are shown in Fig. 21.

Ln(Rswitch) versus Time
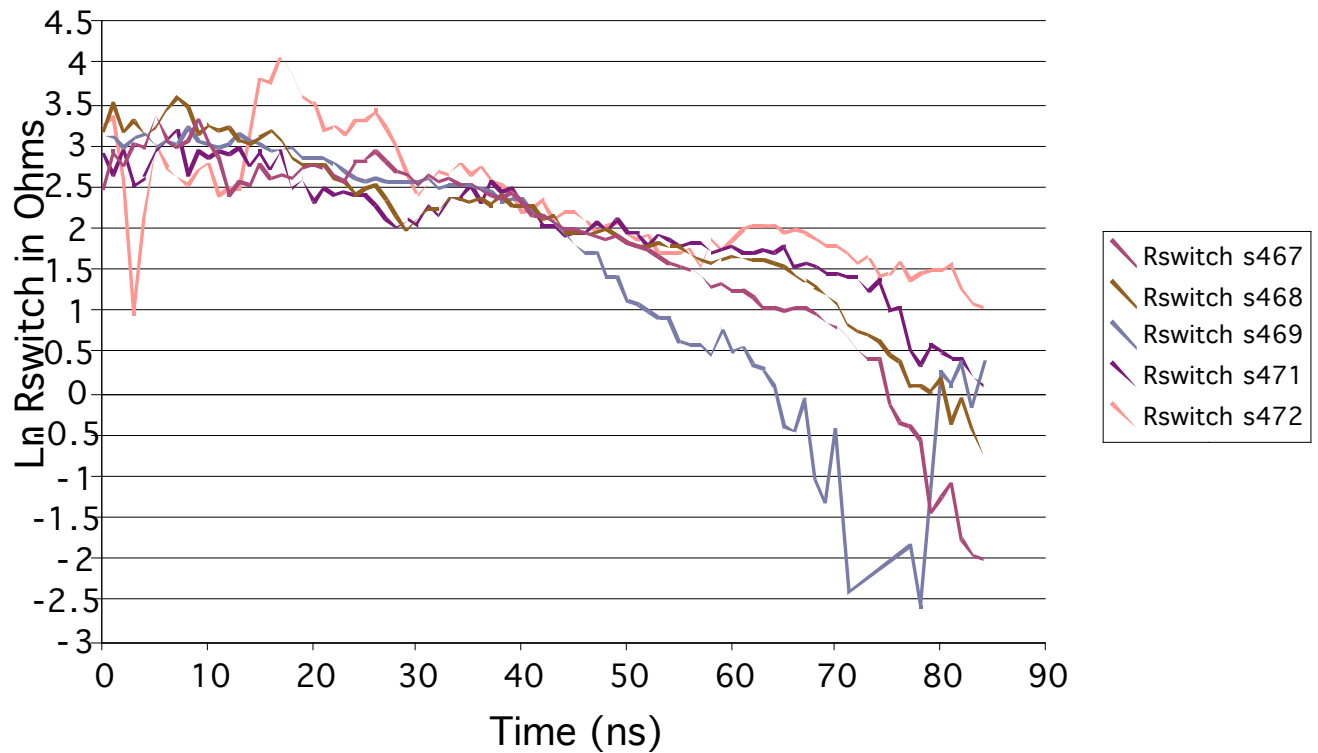
Fig. 21: Natural logarithm of switch resistance versus time for Tesla switch data. The timing has been shifted so that the waveforms are aligned at 10 Ohms.

The resistance falls with one e-fold time in a first stage and then a faster e-fold time for the second stage. Since the MICA impedance for each channel is 1.5 Ohms [ln (1.5) = 0.45], the hold-off time is largely determined by the first stage time and the current rise time is characterized by the second stage. The analysis is summarized in Table 2.

Shot	Switch Electrode	Gap	Hold off time	First Stage e-fold time	Second Stage e-fold time	Current Switched
467	6mm diameter brass	2.5 mm	~100 ns	19 ns	4.5 ns	270 KA
468	6mm diameter brass	4.0 mm	~100 ns	26 ns	10 ns	220 KA
469	6mm diameter brass	5.0 mm	~125 ns	10.5 ns	5.5 ns	100 KA switched on falling voltage
471	6mm diameter Aerodagged brass	4 mm	~100 ns	32 ns	10 ns	200 KA
472	6 mm diameter Aerodagged brass	5 mm	~100ns	24 to 31 ns	25 ns	150 KA switched on falling voltage

Table 2. Tesla switch data analysis

The 100 ns hold-off times and 2.5 mm gap for 600 KV are reasonably encouraging but a ZR_MICA has to hold off 4.5 MV for ~70 ns. The fastest e-folding time for the low impedance needed to conduct the MICA_PF current is about 5 ns. Although this performance is surprisingly good for a first attempt, the switch rise time would severely limit MICA performance. Developing an adequate vacuum switch is the critical path to developing a successful MICA for ZR. Hermes III could be used in a safe, low voltage and under-matched mode to provide the 4.5 MV source for exploring the vacuum switch performance at ZR voltages.

Until a high-performance vacuum switch is available, we will use an idealized switch with a 1 nanosecond exponential fall time of the resistance. A somewhat longer e-fold time would not be detrimental and may even further reduce the electron losses in the MICA-PF.

We conclude that the physics issues for MICA--to the extent that they are currently understood--do not preclude MICA working successfully. The parameters for the MICA load line, Zflow, and minimum MITL gap to avoid closure have been incorporated into the SCREAMER simulation of the ZR MICA.

SCREAMER Model

The baseline (Version 5) design was modeled with the circuit code SCREAMER using the following as inputs:
1. The MICA and load is a simple replacement for the ZR MITLs, so the baseline power pulse from ZR after the vacuum stack is available for driving the MICA. Although we used the 2005 version of the ZR source voltage for the design iterations, we used the 2006 version distributed by Struve, Harjes, and McDaniel on 09/12/2006 for the final simulations. Both have 0.179 Ohms source impedance and include the water transmission lines and the insulator inductance.
2. The nine spiral lines with a constant 1.5 cm gap will work without closure during the entire duration of the energizing pulse.
3. The 27 vacuum switches will close as required.
4. The composite of the electromagnetic waves and electron flow in the spiral lines and the electromagnetic waves radiating from the switch points are not pathological, i.e. the voltage drop is such that the net magnetic field maintains magnetic insulation, as shown in the Quicksilver simulations.
5. The MICA_PF line impedance equals 0.64 times the vacuum wave impedance of the MITL from which it is powered, as predicted in the Quicksilver simulations.
6. The convoluted disk feed of 27 tapered transmission lines with a 3 mm vacuum gap and mating to a disk feed with a minimum gap of 1 mm, can be built and aligned as a unit and does not break down during the <50 ns output pulse.
7. The Z_{flow} losses agree with the Z_{flow} losses in the MITE tapered transmission line experiment, i.e. $Z_{flow} = 0.79$ x minZo, where $minZ_o$ is the minimum vacuum wave impedance of the power feed.
8. The resistive wall losses are not much worse than the Stygar model that is incorporated in SCREAMER and used in this calculation.
9. The 1 mm gap of the disk feed and of the can around the target does not cause current shunting during the drive pulse.

SCREAMER has three relevant limitations for simulating MICA performance:
1. SCREAMER precludes connecting side branches from the main branch back into the main branch,
2. SCREAMER does not correctly handle MITL or Zflow models with side branches originating in VENDSOURCEs, and
3. SCREAMER routines compute only the last listed SPH or CYL model to provide the pinch dynamics, so multiple implosions are not post-processed correctly.

Therefore, a consistent calculation requires the following four steps:
1. Computation of the effective currents delivered by each of the three MICA_PFs into the equivalent load--with the program provided in Appendix A

2. Post-processing the output of that program to generate the input voltage sources for MICA_PF 1 and MICA_PF 2 to drive a common load with MICA_PF 3. This spreadsheet takes the output of the A computation and computes the effective source voltage of MICA_PF 1 and MICA_PF 2. Each voltage source equals the voltage after the switch resistance (but before the switch inductance) plus the product of the current through the switch times the MICA_PF source impedance, which equals 0.64 times the vacuum wave impedance of the spiral MITLs. For ZR, each nine-line MICA_PF has a source impedance of 0.64 x 0.239 = 0.153 Ohms.
3. Computation of the combined currents delivered by the three MICA_PFs into a common load with the program provided in Appendix B
4. Post-processing the output to extract the pinch dynamics. The load voltage and current and the formula for the inductance of a quasi-spherical pinch are used to compute the flux LI, the inductance L, the change in inductance dL/dt, the radius of the current sheet, the pinch velocity, and kinetic energy of the imploding load.

The appendices are internally documented. The post-processing spread sheets are available from Pace VanDevender.

SCREAMER Results

Eight combinations of
- two MICA_PF impedances (minimum vacuum wave impedance = 1.0 Ohm or 0.5 Ohm)
- two geometries of QSDD2 capsules (half-polar angle = 30 degrees or 45 degrees)
- two versions of the vacuum switch at the end of the spiral transmission lines to the MICA_PF 3 (no switch and switch functions as a prepulse switch)illustrate the predicted performance of ZR MICA driving QSDD2..

One-dimensional LASNEX simulations of a QSDD2 capsule were performed to tentatively identify the benefit of these options are worth the associated risks. A 2.5 mm radius QSDD2 (beryllium/gold/cryo-DT/gaseousDT , which is discussed in the next section) was chosen for the comparison. The yield as a function of cryo DT mass is shown in Fig. 22.

1-D Yield for ZR-MICA QSDD2 Capsules
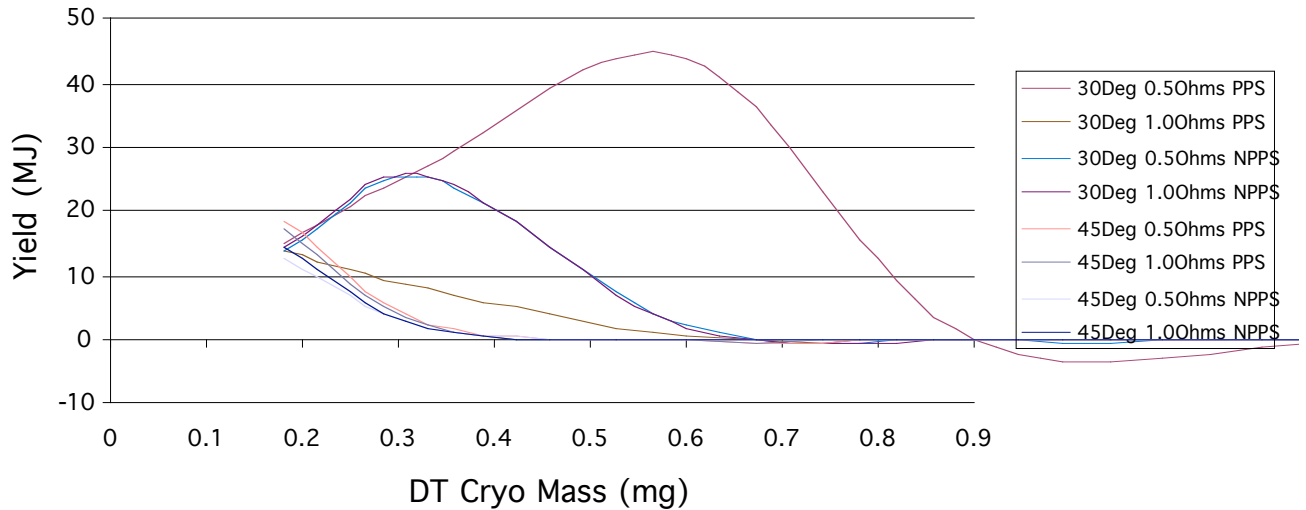
Fig. 22: One-dimensional yield versus cryo DT mass for a 2.5 mm high-adiabat capsule for each of 8 MICA waveforms.

The results show that the prepulse (without the MICA3 switch) did not strongly affect the yield but it does introduce a risk of plasma formation and expansion. Therefore, we will use a MICA3 switch and close all switches at 174 ns--13 ns after the self-magnetically insulated power pulse has reached the end of the spiral MITLs—for all high-adiabat capsules. We will use the MICA3 switch as a prepulse switch and vary its timing to produce the foot for pulse shaping the drive for low-adiabat capsules.

The higher inductance of the 45 degree capsule reduces the current by 10%. The lower currents of the 45 degree configuration significantly lowered the 1-D yield. Therefore, we will adopt the 30 deg configuration as the baseline configuration. If mixing from the two-dimensional simulations with realistic walls is prohibitive, the 45 degree configuration will be reconsidered.

SCREAMER simulations of the baseline design (with a MICA_PF, minimum vacuum wave impedance of 1.0 Ohms) for driving high-adiabat capsules and wire arrays and of an alternative 0.6 Ohms for driving low-adiabat pulses-shaped capsules, were performed with the FY2006 predicted open circuit voltage for ZR as the input. The resulting currents are shown in Fig. 23 and 24 respectively.

**Summary of Currents
with Min Zo=1.0 Ohms**

Legend: ILOAD, IMICA1, IMICA2, IMICA3, I_INTO_ZFLOW, IZFLOW_LOSS
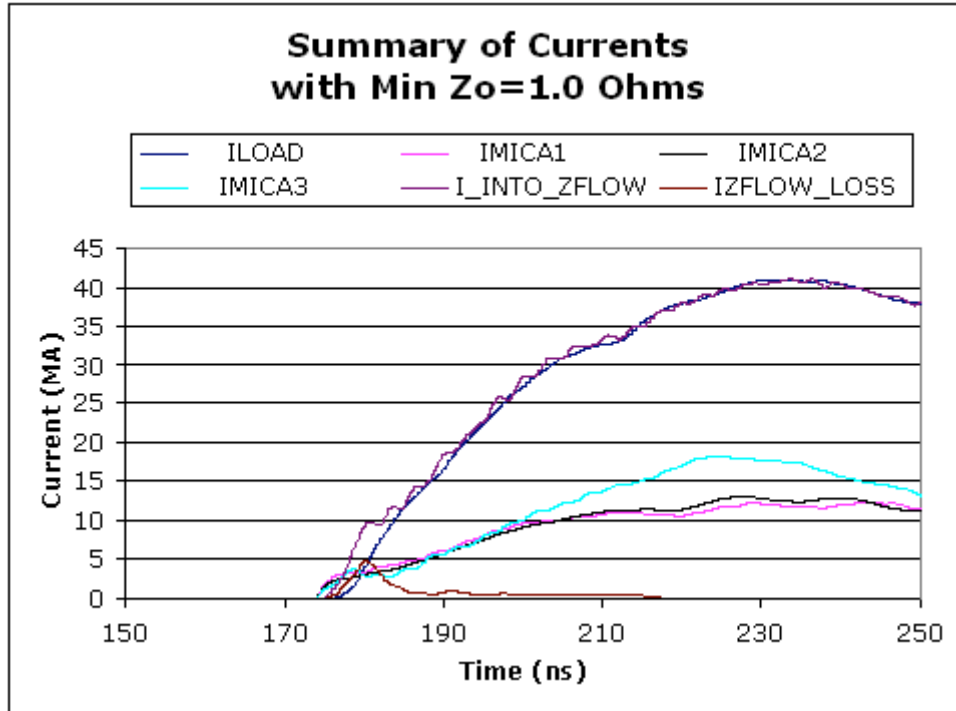
Fig. 23: Currents driving a 30-degree half-angle high-abiabat capsule with 1.0-Ohm minimum impedance MICA_PF. The low electron flow makes this the desired configuration for driving wire arrays.

Currents in Version 7 with 9.9 mg 2.5 mm Capsule
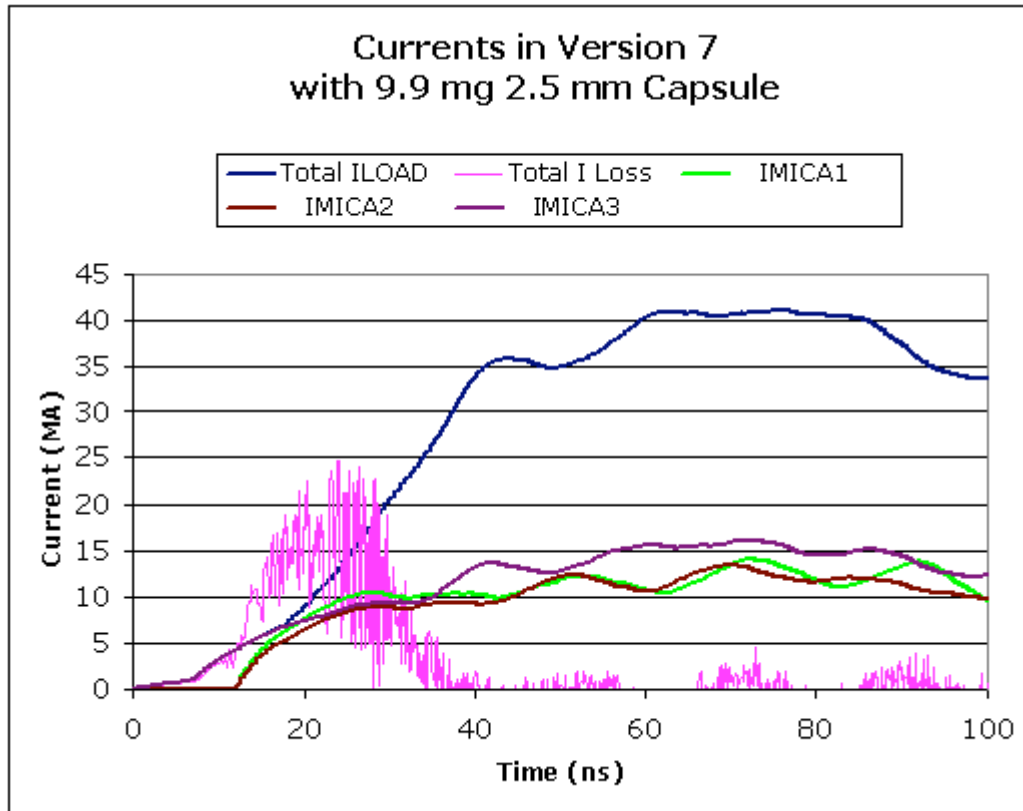
Fig. 24: Currents driving a 30 degree half-angle, low-abiabat capsule with a 0.6 Ohms minimum impedance MICA_PF. The pulse shape is achieved by switching MICA3 at 162 ns and switching MICA1 and MICA2 at 174 ns.

Note the current rise time is somewhat shorter and the Zflow loss current is significantly higher for the 0.6-Ohm geometry compared to the 1.0-Ohm geometry but the current rate of rise continuously increases to give a smoothly increasing magnetic pressure on the capsule.

MICA Version 5 is the baseline design. Version 6 of the MICA for ZR has the same 1.0 Ohm minimum vacuum wave impedance MICA Power Feeds and the same closing switch at the MICA3 position at the end of the spiral MITLS. Version 6 has a more versatile and maintainable tri-plate MITL design for the MICA_PF. To properly account for the coupling with the spiral MITLs, each capsule configuration must be simulated with the coupled SCREAMER programs in Appendices A and B. However an approximate equivalent circuit will help others quickly investigate the utility of ZR-MICA for a variety of loads.

Approximate Equivalent Circuit

The SCREAMER tools in Appendices A and B were used with constant resistance loads to compute the effective load line. The results are shown in Fig. 25.
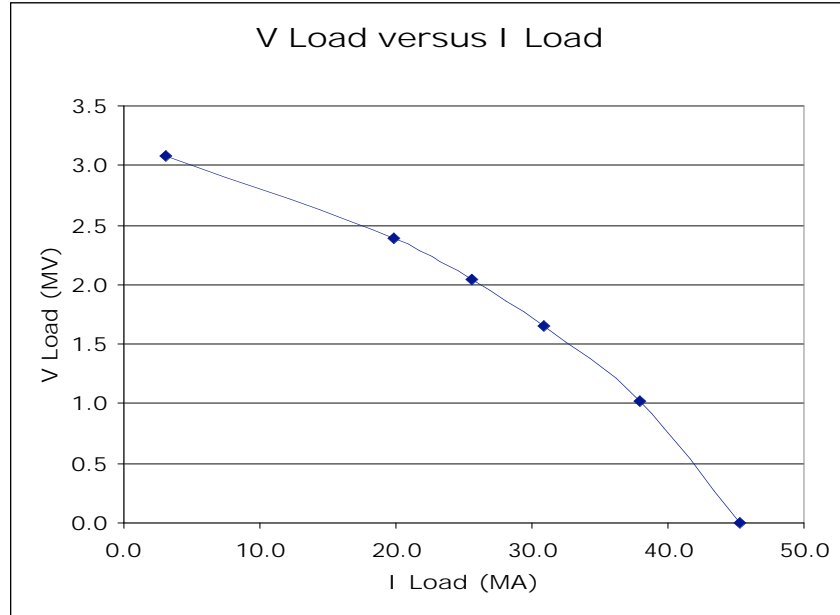
Fig. 25: Effective Load Line for ZR MICA Version 5 with constant resistive load.

The effect of the Z_{flow} losses is evident as the load resistance is increased above 0.06 Ohms. The effective forward going source voltage $2V_o$ at the input to the disk feed, i.e. MICA-PFs and their Z_{flow} losses, was derived by computing $2V_o(t, R_{load})$ for the three intermediate load resistances (0.27 Ohms, 0.536 Ohms, and 0.80 Ohms) and choosing the single source impedance that minimized the standard deviation of the first 60 ns of significant current for the three waveforms. A source impedance of 0.080 Ohms produced the 1.2% minimum standard deviation between the three waveforms for $2V_o(t)$. The resulting effective waveform for the baseline ZR_MICA is shown in Fig. 26 as smoothed version through the ringing—which may well be an artifact of the discreteness of the SCREAMER simulation but more analysis is need to know for certain.

Fig. 26: Effective MICA_ZR source voltage for the baseline configuration.

The optimum implosion time to couple maximum energy into the imploding mass is ~40 to 50 ns, which means that the 1mm gap of the vacuum feed only has to remain open for that time.

Calculations with the following piecewise smooth expression in Table 3 for 2Vo in series with a 0.080-Ohm source impedance and a 1.2-nH feed inductance provides an approximate drive for examining the utility of ZR_MICA.

Time(ns)	2Vo(MV)
0	0.00
5	2.60
13	2.60
16	3.10
21	3.30
23	3.40
41	4.20
56	4.00
79	3.30
110	3.20
124	3.10

Table 3. Approximate ZR_MICA drive

Conclusion on MICA

The major risk resides in developing a high performance vacuum switch and in qualifying the 1 mm vacuum gap at 18 MA/cm linear current density for the 50 ns implosion time in the radiation environment of the load. The QSDD2 load produces a modest 10 to 40 eV black body source during the implosion and is particularly well suited to ZR-MICA. The available data, 3-D Quicksilver simulations, SCREAMER circuit simulations, and analysis indicate that a MICA can enable a significantly expanded experimental space for ZR and help meet expectations for precision, capacity, and capability if the two major risks are mitigated by further research. It is well matched to quasi-spherical direct drive capsules and is capable of providing modest pulse shaping.

The next step in the development of a MICA for ZR should be additional experiments on the switch using Tesla and Hermes III, the mechanical design of the tri-plate MICA-PF for Version 6, a more detailed cost estimate of the MICA system (to replace the preliminary estimate by the engineering team of $2M), and design of a Hermes III-driven single-MICA module at the full voltage and current of a ZR MICA.

IV. QSDD2—Quasi Spherical Direct Drive Single Shell Capsules

The Desjarlais conductivities [17] for beryllium, gold, and the Lee, Moore, Desjarlais conductivity [18] for deuterium DD (assumed to be the same for deuterium-tritium DT) makes realistic simulations of a single–shell, quasi-spherical direct drive capsules possible. We referred to these capsules as QSDD2 capsules. The perceived features and issues for this class of capsule are shown in the Table 4.

Features	Issues
Magnetic drive avoids the 84% inefficiency of converting to x-rays, so more energy goes into the pusher. The resulting higher energy in the fuel reduces the requirement for implosion velocity and for convergence ratio.	The $1/\cos^2\Theta$ dependence of the drive pressure means that the mass density has to be tailored with angle from the equator. Since the DT ice has to be spherical, the Be pusher has to be shaped. The ratio of the thickness of the Be at 45 degrees to that at 0 degrees should be 2.0. We need to determine the tolerable variation in the initial shape of the capsule to specify the fabrication requirements adequately.
Drive does not depend on photon diffusion through plasma.	The symmetry of the drive has to be directly ensured by the design of the driver. Asymmetries from the power flow are not smoothed out by photon diffusion. We need to address what fraction of the driver energy is coupled to the capsule for a realistic accelerator design.

Pulse shaping occurs naturally because the magnetic pressure increases with decreasing radius. The magnetic drive pressure for 60MA through a 0.254 cm radius capsule after converging a factor of 12 is 8×10^{14} Pa--which is equivalent to an ablation pressure of 868 eV.	The pulse shaping is an integral feature of the target implosion and can not be controlled independent of radius. Magnetic insulation of the current must continue to be effective as the capsule implodes to about 200 microns radius.
Unlike radiation drive, which has the ablation pressure independent of the radius for constant temperature, the drive pressure continues to increase as the capsule implodes so the PdV work is increased by about 50%. The PdV work at a convergence ratio of 12 in the 60 MA target is 1.4 MJ, compared to 1 MJ absorbed by the capsule in the x-ray drive and about 200 KJ in the fuel.	We need to determine the fraction of the PdV work gets into the fuel.
The ramping pressure profile helps compression but changes the dynamics of the normal multi-shock hot-spot ignition capsules.	We need to investigate how the magnetically driven shocks and adiabatic compression can create a low adiabat compression.
The current penetrates into the Be and DT to heat the core, which is then compressed.	We need to study how the combined effects of Joule heating, shock heating, and adiabatic compression can raise the temperature enough to ignite the compressed fuel.
The conical electrodes allow a fill hole near the outer DT radius and the motion of the Be sweeps past it and takes it out of the implosion.	The metal walls are a source for mass loss during the implosion, will deform, reducing the peak fuel density, and may provide material to mix with the fuel. We need to understand and mitigate the wall interaction.
DT fuel will plate out on the cones to reduce the tendency for mixing of the cone material with the core fuel.	The cold fuel may provide an anti-mix layer on the metal walls and make up for the mass lost to the walls, and hence, help the implosion but it may cool the hot spot.
The mass is not ablated, so more of the PdV work is, in principle, available for compressing the fuel and keeps the in-flight aspect ratio low to reduce the effect of the Rayleigh-Taylor instability.	The beryllium absorbs energy from the PdV work as well. We need to know what fraction is absorbed by the DT and if the tamping effect of the Be is significant in increasing the burn fraction.

The shortest wavelength magnetic, Rayleigh Taylor instability is cut off by the diffusion of the current into the pusher. The dominant mode is the one that matches the gradient in the density. Hussey, et al, [19] showed that the growth was not disruptive for drive times of <60 ns—the drive times proposed for QSDD2.	The stability of the sheath will be carried out in subsequent investigations.
The long wavelength Rayleigh Taylor instability could destroy the imploding shell.	2-D simulations were conducted in this study to assess this issue.
The decelerating pusher is Rayleigh Taylor unstable and may break up the shell and mix pusher material with the DT.	2-D simulations were conducted in this study to assess shell-breakup issue. The dynamics of the decelerating shell is compared with models from the literature to provide a preliminary assessment of the potential for catastrophic mix from the pusher.

Table 4: Perceived features and issues for QSDD2 capsules

We investigated two classes of capsules with one-dimensional LASNEX simulations to address these issues and prepare for more realistic two-dimensional simulations with LASNEX and MACH2. In parallel with the LASNEX simulations, we performed two-dimensional simulations with MACH2. The two classes of capsules are 1) single-shell cryogenic capsule with a all beryllium pusher to provide a low-adiabat compression and hot spot ignition and 2) single-shell cryogenic capsule with a beryllium-on-gold pusher to provide a high-adiabat compression and hot spot ignition by compression of the hot plasma. The first one is scalable to high-gain; the second one is useful for intermediate-term applications like radiation effects simulation.

Both capsules were simulated with the LLNL recommended parameters for simulating inertial fusion capsules. The analysis of the results follows that of Herrmann, Tabak, and Lindl. [20] We gratefully acknowledge the exceptional guidance and tutelage of the Sandia inertial fusion design team—especially Steve Slutz, Roger Vesey, Mark Herrmann, Ray Lemke, Kyle Cochran, Mike Desjarlais, Tom Haill, and Peggy Christenson.

One Dimensional Simulations of Low Adiabat QSDD2 Capsules

The low-adiabat capsules had DT gas at 3×10^{-4} g/cm^3 fill density, surrounded by cryogenic DT, surrounded by a beryllium conductor-pusher. Current drives of 60 MA, 40 MA, and 34 MA were examined. The results are shown in Table 5.

Current Drive	60 MA drive with constant 16 MA foot for 14 ns followed by a 10 ns rise to 60 MA and then constant 60 MA	60 MA drive with linearly rising 16 MA foot for 14 ns followed by a 10 ns rise to 60 MA and then constant 60 MA	40 MA drive with linearly rising 16 MA foot for 14 ns followed by a 10 ns rise to 40 MA and then constant 40 MA	40 MA drive with linearly rising 16 MA foot for 14 ns followed by a 10 ns rise to 40 MA and then constant 40 MA	ZR MICA3 with 15 ns rise to 9 MA and 25 ns (~sin^2) rise to 33 MA and then constant.
Outer Radius of DT gas (cm)	0.218	0.218	0.218	0.218	0.218
Outer Radius of cryogenic DT (cm)	0.247	0.247	0.247	0.247	0.247
Outer Radius of Be	0.254	0.254	0.254	0.25	0.25
DT cryo mass (mg)	1.815	1.815	1.815	1.815	1.815
1_D Yield (MJ) for a 45 deg-half angle QSDD2	290	290	238	228	0.135
Percent Burn (%)	53	53	44	42	0.025
Max Ti(Kev)	110	103	76	77	0.372
Total rho-r (g/cm^2)	5.53	4.82	3.1	2.8	2.8
DT rho-r (g/cm^2)	1.88	1.66	1.42	1.44	1.52
DT-gas rho-r (g/cm^2)	0.77	0.33	0.72	0.082	0.82
Convergence Ratio of outer DT cryo radius	15.7	15.64	13.78	13.7	12.7
Maximum implosion velocity of Cryo_DT-Pusher interface (cm/microsecond)	-30.2	-33	-22	-24.4	-18.3
Minimum adiabat (alpha) at maximum implosion velocity	1.86	1.8	1.27	1.48	1.21
Fraction of DT mass on an adiabat > 1.5 times the minimum alpha	46	35	19	22	15
Peter Amendt's Tau factor--(t_burn-t_freefall)/fwhm_burn_width)	-4.3	-5.5	-0.48	-0.88	-0.77
% Clean DT based on integration of David Youngs' criterion for mixed fuel--second integral of 0.14 of cryo interface decelertion.	87	89	81	82	92
Current in Be at 5 ns before burn (MA)	47	47	34	32	27
Current in Cryo DT at 5 ns before burn (MA)	12	13	6	8	6
Current in Gas DT at 5 ns before burn (MA)	1.2	0.42	0.38	0.3	0.4
Pressure from first shock (MB)	2.4	2	4.7	13	7
Burn width (Yield divided by Max burn rate) (ns)	0.052	0.043	0.084	0.081	0.84

Table 5: Key Parameters on the LASNEX 1-D simulations of the low-adiabat QSDD2 capsules

The 1-D simulation results show that the basic dynamics of QSDD2 allow a high performance capsule if the wall effects and the Rayleigh Taylor instabilities are benign or can be mitigated. The 60 MA driver with a 14 ns, 16 MA foot and a 10 ns rise to 60 MA had a 1-D yield of 290 MJ and a 53% burn up. The minimum alpha was sufficiently low (1.90), even though the fraction (fma) of the fuel at >1.5 times the minimum alpha at peak implosion velocity was >35%, to allow the driver to compress the fuel to a rho-r of ~1.7 g/cm^2. Clearly such a driver could achieve useful compression and can heat the compressed plasma to sufficient temperature for ignition. The same is true for the 40 MA driver with a fast (~10 ns) rise time of the main pulse. In fact, the minimum alpha (1.27 to 1.5) and the fma (20%) were better for the 40 MA case and the rho-r of the fuel was still 1.4 g/cm^2. In both cases, the total rho-r of >2.8 was sufficient to tamp the burn and achieve a high burn-up fraction of 40% to 50%.

The fraction of the fuel that remains unmixed, which was predicted from David Young's experimentally derived mix model [21] was >80%. The freefall line crosses the axis well after peak burn in all the 60 MA and 40 MA capsules. Therefore, pusher-fuel mix may not be catastrophic in the QSDD2 design. However, if all of the fuel behind the free-fall line is duded (no burn), the yield drops to 1 to 3 MJ for the 60 MA driver and 0.6 to 1.2 MJ for the 40 MA driver. In all cases, the convergence ratio, as determined from the initial and final positions of the fuel-pusher interface, is 12.7 to 15.7 and is comparable to the convergence ratio in the 2-D results presented below. Based on these results, the QSDD2 capsule would be worthy of experimentation for a ~10ns-risetime, 40-MA driver.

The same capsule cannot be driven by a ~34 MA pulse rising in ~30 ns from the computed currents from the MICA3 and MICA4 configurations for a ZR-MICA without adjusting the capsule parameters. Using a larger radius and lower mass capsule to increase the implosion velocity could make the Rayleigh-Taylor instability a larger issue. Optimizing the low-adiabat capsule for ZR-MICA will be pursued in the next phase of QSDD2 studies by calculations of capsule performance and Rayleigh Taylor stability. Conducting the study requires more sophisticated tools to post process the LASNEX data and those tools are now being adapted to the QSDD2 simulations.

Understanding and mitigating the wall effects and long-wavelength Rayleigh-Taylor instability of the low-adiabat QSDD2 capsule must be done to illuminate the potential for the 60 MA and 40 MA drivers with QSDD2 capsules and perform optimization of the capsule for experiments on ZR.

Two Dimensional Simulations of Low Adiabat QSDD2 Capsules

A series of MACH2 [23] simulations were conducted to improve the understanding of the potential for quasi-spherical direct drive (QSDD) fusion on ZR and future machines. These simulations included zoning-resolution studies of the wall perturbation seen in earlier QSDD simulations [24] at high current. These earlier studies involved the implosion of quasi-spherical ICF targets consisting of a beryllium outer shell, a DT ice shell, and an interior DT gas fill. To compensate for the $1/r^2$ variation in the driving

magnetic field, the outer surface of the beryllium shell was tapered outward so that the thickness at $\pm 45^o$ from the equator was $2.0\times$, $2.1\times$, $2.2\times$, or $2.3\times$ the thickness at the equator. In these simulations a perturbation developed and grew near the wall at $\pm 45^o$. This behavior was detrimental to the implosion since it allowed beryllium shell material to penetrate into the DT fuel and reduce capsule performance. The perturbation develops as the magnetic driving forces at the back of the shell push some material against the wall electrode. This produces a density perturbation near the wall, which grows because of the $1/r^2$ variation in the field. The lower density region is accelerated more than the higher density region. It is pushed to smaller radius than the higher density region. At smaller radius the field is higher and the process continues. One method of mitigating this effect is to use a step in the wall to 'scrape off' the region containing the perturbation. The method was computationally found to be effective in mitigating a similar problem of the SHIVA x-ray generator. [19] The simulation results reported here are to investigate the use of steps on ZR and future machines.

Vertical Zoning Resolution Simulations

The first series of simulations investigated the zoning resolution necessary to resolve the details and effects of the wall perturbation at a sufficient level to mitigate the influence of numerical effects on the development. This series included calculations of a full 90° quasi-sphere at 16, 32, 64, 96, and 128 vertical zones. The capsule was a 2.54 mm radius capsule investigated for x-ray driven fusion with z-pinches [25]. It had a DT gas fill from $r = 0$ to $r = 2.18mm$, a layer of DT ice from $r = 2.18mm$ to $r = 2.40mm$, and a beryllium shell for $r = 2.40mm$ to $r = 2.54mm$. The current drive had a peak current of 60 MA.
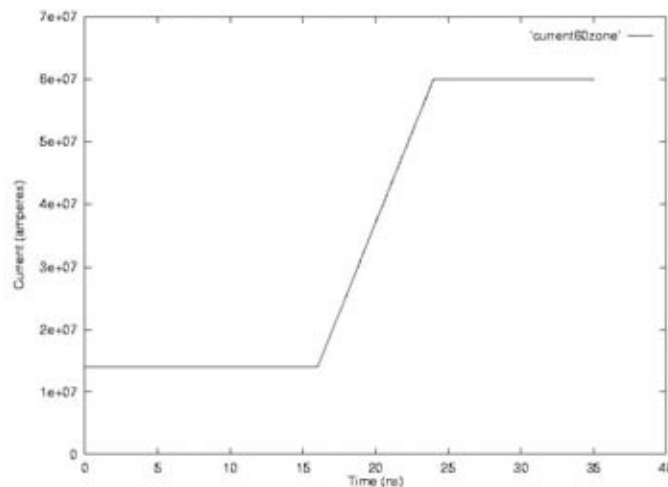
Fig. 27: Current vs. time for zoning study

The perturbation was present in all of the simulations and grew to a significant level at peak compression. The results indicate the radial penetration of the wall perturbation increases with zone number and the vertical dimension of the feature decreases with increasing resolution up to 96 vertical zones. The feature at 128 vertical zones yields basically the same as at 96 zones as shown in Fig. 28.

| 32 vertical zones | 96 vertical zones | 128 vertical zones |
| Fig. 28a | Fig. 28b | Fig. 28c |
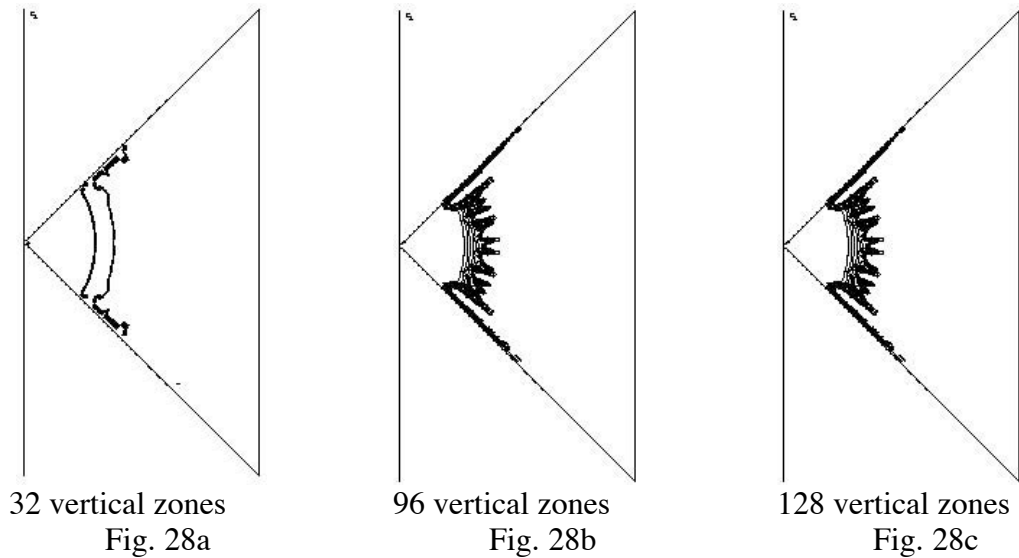
Fig. 28: Mass density contours at 30.0 ns

Step Investigations with 60 MA Model Current Waveform

The next two series were run with model currents for a future machine with a peak current of 60 MA, and a model ZR Magnetically Insulated Current Amplifier (MICA) current wave shape with a maximum current of 40 MA, both current shapes shown in Fig. 29. These calculations investigated the use of a step in the electrode to mitigate the wall perturbation.
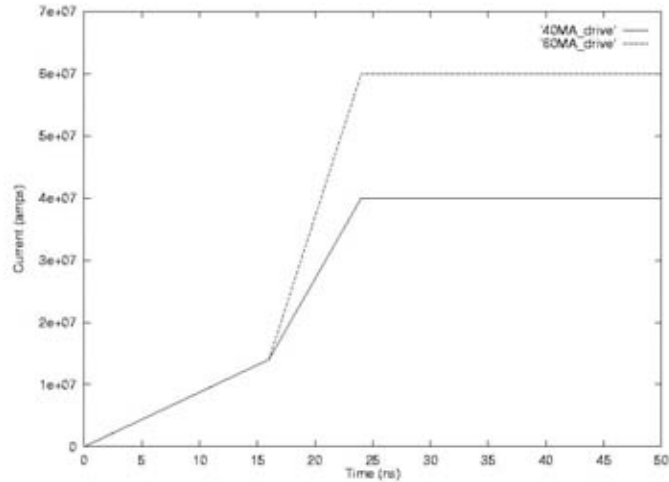
Current vs. time for first step evaluations
Fig. 29: Current Waveform for Zoning Simulations

The 60 MA current waveform (for the model future machine) has a linear rise from 0 to 16 MA in 14 ns and a linear rise from 16 MA to 60 MA between 14 ns and 24 ns, after which it remains constant at 60 MA. The 40 MA current waveform (for a model ZR MICA) has a linear rise from 0 to 16 MA in 14 ns, a linear rise from 16 MA to 40 MA between 14 ns and 24 ns after which it remains constant at 40 MA. In the equatorial plane, the capsule for the 60 MA drive and 40 MA drive is the same 2.54 mm radius capsule used in the zoning-resolution study discussed above. For these simulations the thickness of the beryllium shell at 90° was 2.0 x the thickness at the equator. While this was not the 2.2 x the equator thickness used in earlier simulations, it produced a more pronounced wall perturbation and made the study of the effects of the step easier. These simulations were conducted with 1/2 of the 90° quasi-sphere or a quasi-sphere that went from 0° to 45°. This simplification and running with a coarser mesh (40 vertical zones for the 45 degree simulation rather than the 96 for a full 90 degree simulation) reduced the computational time and allowed a larger number of parameters for the step to be investigated.

Two different step geometries were investigated. The first had the step at 135° to the outer part of the top electrode and perpendicular to the equator, Fig. 30a. This configuration is similar to that used on SHIVA. The second had the electrode at 90°, perpendicular to the outer part of the top electrode, Fig. 30b.

47
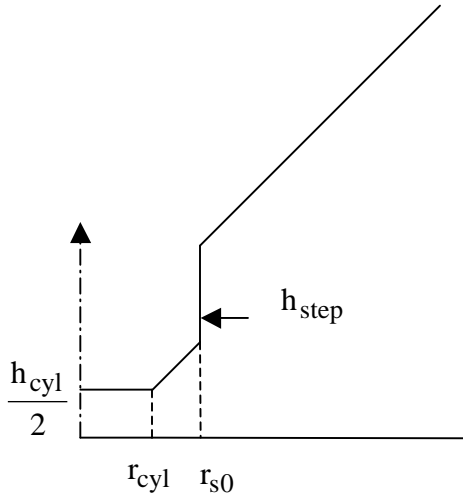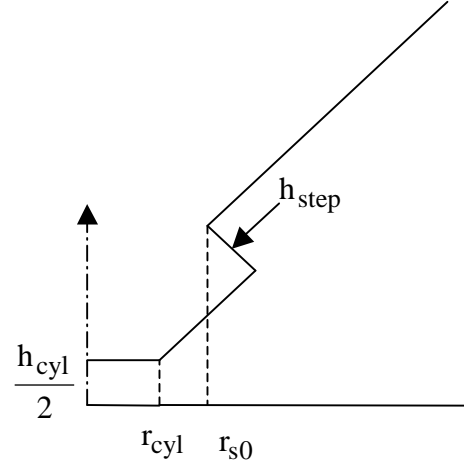
Fig. 30a 135° step   Fig. 30b 90° step

Fig. 30: Step geometries

Parameters varied for these simulations included the half-height of the central cylinder, $\frac{h_{cyl}}{2}$, the radius of the central cylinder, r_{cyl}, the location of the tip of the step measured as r_{s0}, the radius of the step corner projected to the equator from the top electrode, and the height of the step. The step height h_{step} is the length of the step from the outer electrode to the inner electrode. For the 135° step, this is the vertical distance on the z-axis. The initial step height and location were taken from estimates of perturbation development for simulations without a step.

Results from the 135° geometry showed the step did influence the development of the perturbation. The perturbation was removed and for step locations, r_{s0}, inside 1.15 mm the perturbation did not show significant redevelopment. At this angle the material that was 'scrapped off' flowed down the back of the beryllium shell. This flow introduced additional perturbations on the back of the shell, and reduced the final shell velocity since the driver had to reaccelerate this mass in an inward radial direction. The mass flow was not an issue for the SHIVA implosions. For these radiation production implosions the principal aim was to produce a sharper radiation pulse by creating a straight leading edge to the plasma. The location of the step was early in the implosion and the redevelopment time longer which meant the velocity reduction was less of an effect. At the higher current for QSDD2, the redevelopment time is shorter and the velocity requirements are higher. In addition, the perturbations introduced by the mass flow could aggravate the Rayleigh Taylor instability for the beryllium shell.

Results for the 90° step were more promising. Again the perturbation was removed and for step locations r_{s0} inside 1.15 mm the perturbation did not show significant redevelopment. The mass stagnated on the step remained compressed against the step resulting in higher velocities for this case. Results typical of this geometry are shown in Fig. 31.

No step   Perpendicular step: h_{step} = 0.2mm r_{s0} = 0.85mm

t = 31.5ns   t = 29.0ns   t = 31.5ns

Fig. 31a   Fig. 31b   Fig. 31c
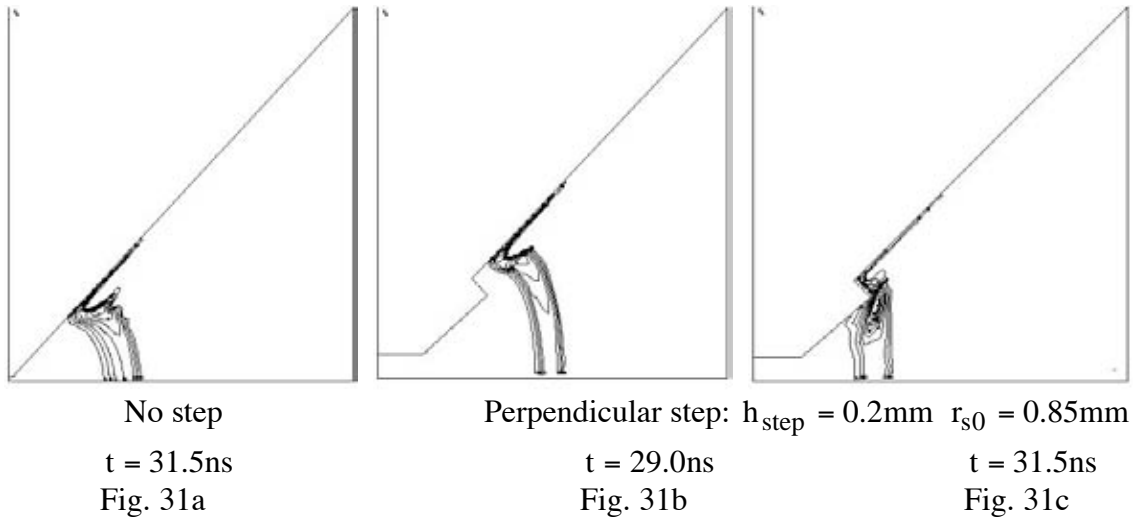
Fig. 31: Mass density contours

Fig. 31a shows the imploding beryllium shell at 31.5 ns with straight electrodes. The wall perturbation is very evident. Fig. 31b shows the perturbation at 29.0 ns before the sell encounters the step. Fig. 31c shows the shell after encountering the step at 31.5 ns. It is clear that the perturbation has been removed and does not redevelop for this case. Table 6 illustrates the effect of the step on the peak DT neutron production rate and step location.

Geometry	DT production rate
No step	1.67×10^{25} / sec
Step at 0.75 mm	3.06×10^{25} / sec
Step at 0.85 mm	3.18×10^{25} / sec
Step at 0.95 mm	2.67×10^{25} / sec

Table 6. Peak DT neutron production rate as a function of step location with 0.2 mm step perpendicular to the electrode and 60 MA model current waveform

Step Investigations with 40 MA MICA ZR Model Current Waveform

For the 40 MA model MICA waveform the results were similar but in general the peak DT neutron production rates were lower because the lower current resulted in lower final shell velocities. The results here were more sensitive to step location and height changes.

Again the height and location of the step was varied to get a coarse performance grid. As before the perturbation was removed and for step locations r_{s0} inside 1.15 mm the perturbation did not show significant redevelopment. Again the mass stagnated on the step remained compressed against the step. The perturbation and instability development were reduced for this lower current drive. This can be attributed in part to the lower current reducing the acceleration.

The initial calculations were done for the same 2.54 mm radius capsule [25] described above but simulations of this capsule had very low velocities at this lower current. Since the Rayleigh-Taylor stability did not appear as strong at the low current, the target was modified by reducing the thickness of the beryllium shell from 2.54 mm to 2.50 mm. The modified target had a DT gas fill from $r = 0$ to $r = 2.18 mm$, a layer of DT ice from $r = 2.18 mm$ to $r = 2.40 mm$, and a beryllium shell for $r = 2.40 mm$ to $r = 2.50 mm$. With this change, the velocity of the implosion increased slightly. Fig. 32 shows the beryllium material contours for a 0.25 mm step located at $r_{s0} = 1.05 mm$.
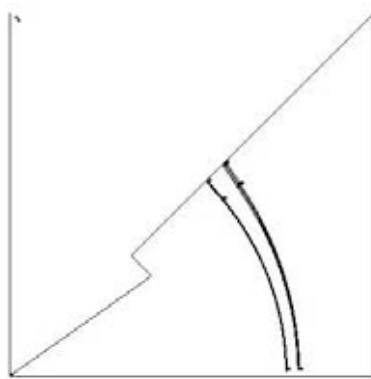
Time = 0.0 ns
Fig. 32a
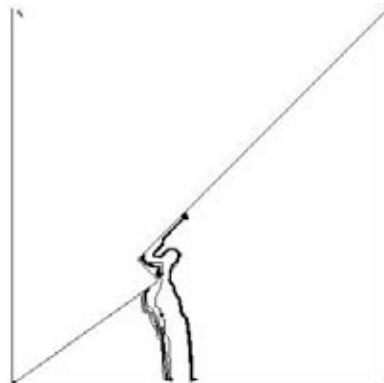
Time = 30.0 ns
Fig. 32b
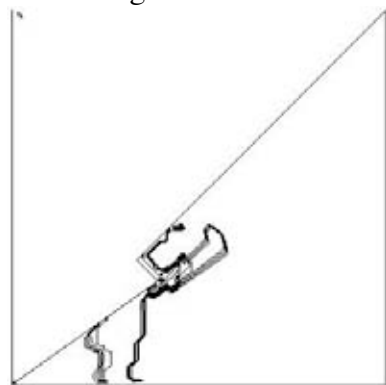
Time = 32.0 ns
Fig. 32c
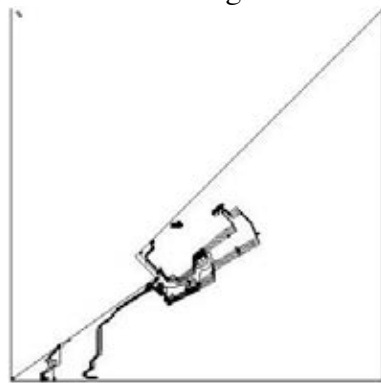
Time = 35.0 ns
Fig. 32d

Fig. 32: Beryllium material contours for a 40 MA model MICA ZR implosion
Step perpendicular to the electrode at $r_{s0} = 1.05 mm$ of height $h_{step} = 0.25 mm$

Table 7 illustrates the effect of the step on the peak DT neutron production rate for this 0.25 mm step and several step locations.

Geometry	DT production rate
No step	$5.94 \times 10^{24} / \sec$
Step at 0.75 mm	$1.35 \times 10^{24} / \sec$
Step at 1.05 mm	$2.47 \times 10^{25} / \sec$
Step at 1.25 mm	$6.11 \times 10^{23} / \sec$

Table 7. Peak DT neutron production rate as a function of step location for 0.25 mm step perpendicular to the electrode and 60 MA model current waveform

These and other results indicate an increased sensitivity to step location for this lower current system.

The final simulations represent a more limited series using the circuit model MICA current waveforms. There are two waveforms used for these preliminary calculations, which we have denoted as MICA3 and MICA4.

MICA3:   10.0 Ohm MITLs with no prepulse switch
MICA4:   0.5 ohm MITLs with a prepulse switch
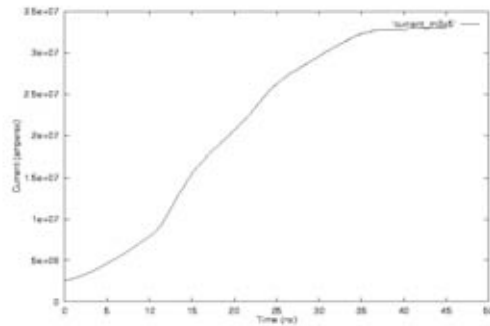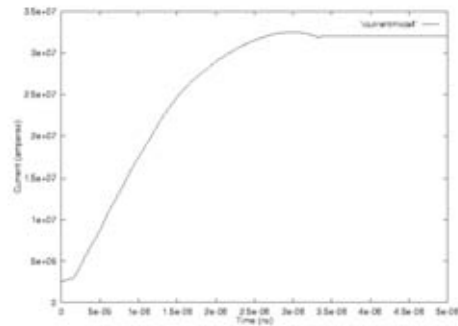
Fig. 33a: MICA3   Fig. 33b: MICA4
Fig. 33: MICA circuit current waveforms

MICA3 rises to a peak current of 33 MA and MICA4 rises to 32 MA.
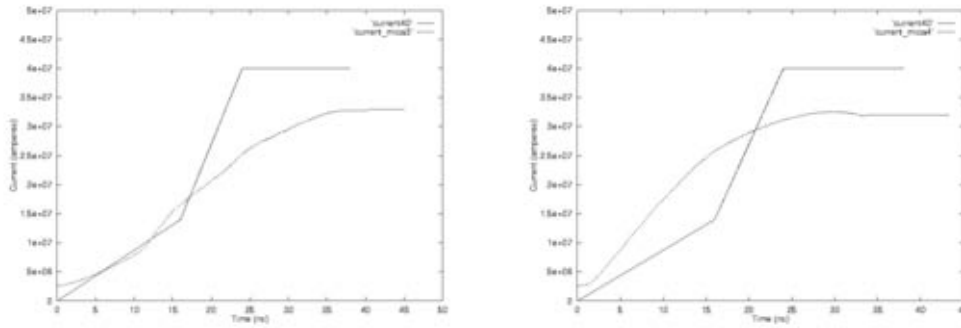
Fig. 34a: MICA3 and MICA model   Fig. 34a: MICA4 and MICA model
Fig. 34: MICA model and MICA circuit current waveforms

The MICA3 and MICA model, Fig. 34a, shows the current waveform is very close for the first 15 ns. After that the model current rises much faster and to a higher level than the MICA3 circuit model. For the MICA4 and MICA model, Fig. 34b, the MICA4 current is higher for the first 20 ns, then the MICA model current is larger one.

Investigations using these circuit waveforms are in the early stages. In the simulations run to date, the wall perturbation is greatly reduced at lower current and lower zoning resolution used for the studies discussed above. Fig. 35 shows the perturbation for the no step case, and shows much later development of the wall perturbation
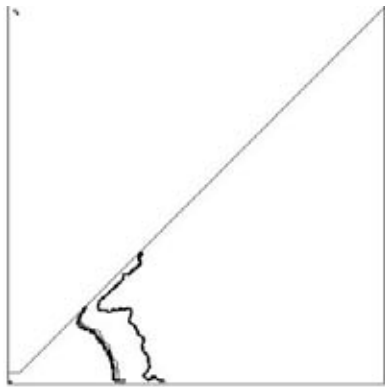
MICA3 no step - Time = 36.0 ns   MICA4 no step - time = 28.0 ns
Fig. 35a   Fig. 35a
Fig. 35: Wall perturbations for MICA circuit current waveforms
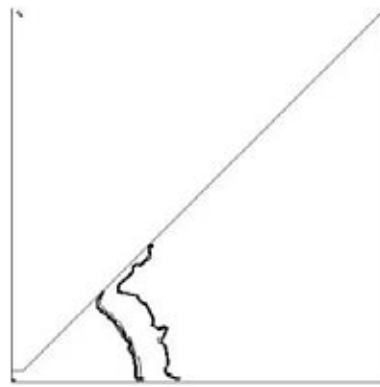
For the step geometries calculated to date the steps again are effective in 'scraping off' the wall perturbation as shown in Fig. 36 and 37. The results to date, however, are not sufficiently complete to identify a step location/height combination that produces a peak DT neutron production rate larger than the no step case summarized in Tables 8 and 9.

52
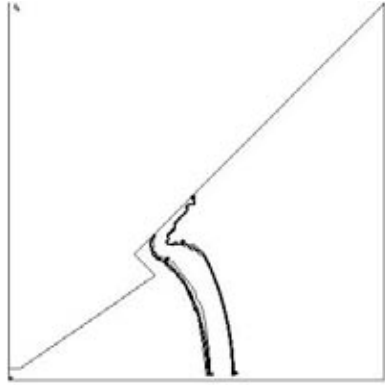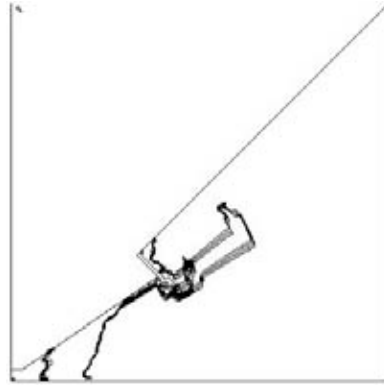
Time = 30.0 ns   Time = 40.0 ns
Fig. 36a   Fig. 36b
Fig. 36: Beryllium material contours for MICA3 ZR implosion
Step perpendicular to the electrode at r_{s0} = 1.05mm of height h_{step}=0.25mm
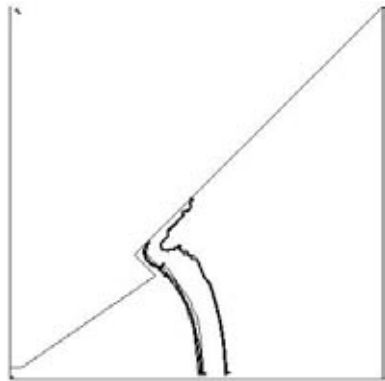
Time = 24.0 ns   Time =33.0 ns
Fig. 37a   Fig. 37a
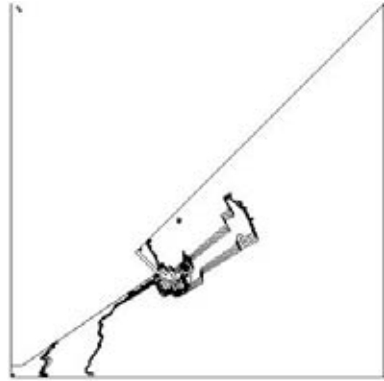
Fig. 37: Beryllium material contours for MICA4 ZR implosion
Step perpendicular to the electrode at r_{s0} = 1.05mm of height h_{step}=0.25mm

Step location	DT production rate
no step	1.65×10^{24} sec^{-1}
step at 1.05mm	6.72×10^{22} sec^{-1}

Table 8. Peak DT neutron production rate as a function of step location,
0.25 mm step perpendicular to the electrode with MICA3 circuit current waveform

Step location	DT production rate
no step	$7.325 \times 10^{23} \sec^{-1}$
step at 0.75mm	$5.47 \times 10^{22} \sec^{-1}$
step at 1.05mm	$9.56 \times 10^{22} \sec^{-1}$
step at 1.25mm	$5.54 \times 10^{22} \sec^{-1}$

Table 9. Peak DT neutron production rate as a function of step location, 0.25 mm step perpendicular to the electrode with MICA4 circuit current waveform

:
The basic conclusions at this time for the MICA ZR circuit current waveforms are
      a. The wall perturbation grows more slowly at lower current:
      b. Final velocities are lower at the lower current
      c. The step is effective in 'scraping off' the wall perturbation.
Too few simulations have been completed to date to say whether the step can improve the neutron production rate.

Summary of MACH2 Simulation Results

MACH2 simulations indicate that 96 vertical zones for a 90 degree simulation provide adequate zoning to resolve the details of the wall perturbation. In simulations with 32 vertical zones, the feature is clearly observable and growth is significant. Using 32 vertical zones is reasonable for parameter surveys. Future results with the recommended zoning should be further investigated at higher resolution to be certain that the simulations adequately resolve the effects.

At 40 vertical zones a series of simulations were carried out to investigate the effects of electrode steps in reducing or eliminating the wall perturbation. Steps in the electrode do change the behavior of the implosion and can 'scrape off' the wall perturbation. This effect was seen for all current drives investigated (60 MA model for a future accelerator, 40 MA model for the MICA ZR accelerator, and circuit model MICA ZR waveforms). The steps produced increase neutron yield rate and yield on the 60 MA and the 40 MA model for the MICA ZR. To date too few simulations have been completed using the circuit model MICA ZR waveforms to see if performance can be improved for the current profiles.

One Dimensional LASNEX Simulations of a High Adiabat Capsule for ZR-MICA

Although adapting the low-adiabat capsule to the longer current rise time of ZR with a MICA is the main approach, we investigated an alternative approach with a high-adiabat QSDD2 cryogenic capsule. The capsule has a gold layer between the beryllium and the cryogenic DT to impede Bremsstrahlung losses from the DT and lower the temperature

for igniting the fuel. The outer radius of the beryllium was 0.0250 or 0.0450 cm. The radius of the gold/DT interface and the CryoDT/GasDT interface were adjusted to vary the mass of the DT and total capsule mass. The current drive was either an idealized 40 MA drive rising from 0 in 15 ns or the output, shown in Fig. 23, from ZR_MICA with 1.0 Ohm minimum vacuum wave impedance in the MICA_PF. The results are summarized Table 10.

The capsule driven by the idealized 40 MA, 15 ns rise time current pulse has reasonable performance but it is not as good as the low adiabat capsules discussed above. However, all of the ZR-MICA capsules have a high adiabat of 13 to 46, which increases with fuel mass. The high adiabat arises from the current driven explosion of the gold shell in the first 10 ns of the current drive and the subsequent relaxation of the first pressure pulse before the main current-driven compression arrives at the gold-cryo interface. All capsules have a large fraction of their fuel at greater than 1.5 times the minimum alpha (minimum adiabat at peak implosion velocity). The fraction of the fuel in the ZR-MICA capsules that is expected to be unmixed, based on the analysis by D. L. Youngs [21] varies from 46% to 76% and is much lower than in the low-adiabat capsules.   More disturbingly, all the ZR-MICA capsules have a positive (bad) value of Amendt's fall-line parameter tau [22], which varies from 0.29 to 1.55. These capsules have to be considered high risk.

We will apply the Youngs' mix model to the non-cryogenic case of a beryllium quasi-spherical shell coated on the inside with gold and filled with DT gas in a subsequent LDRD report. The single shell filled with DT gas has application as a moderate yield system and as a weapons effects source.   We also mention that the gold inner shells of the double shell systems presented in section II have good fall line behavior and some tolerance to mix.

Summary of high-adiabat capsule simulations

Although 1-D simulations of the high-adiabat cryogenic capsules show significant 1-D yields with a ZR-MICA, they are very susceptible to mix and must be considered high risk. Adaptation of the low-adiabat cryogenic capsules to the ZR-MICA drive should have a higher priority in future work. Non-cryogenic gas capsules will be investigated further.

Current Drive	Idealized 40 MA Drive rising from 0 to 40 MA in 15 ns and 30 deg half-angle capsule	ZR-MICA Current Drive shown in Figure 23 with 2.5 mm radius capsule	ZR-MICA Current Drive shown in Figure 23 with 2.5 mm radius capsule	410 ZR-MICA Current Drive shown in Figure 23 with 4.5 mm radius capsule	729 ZR-MICA Current Drive shown in Figure 23 with 4.5 mm radius capsule
Outer Radius of DT gas (cm)	0.234564	0.241	0.2404	0.44639	0.445726
Outer Radius of cryogenic DT (cm)	0.242363	0.24247	0.24247	0.44794	0.44805
Outer Radius of gold (cm)	0.24263	0.24277	0.24277	0.44804	0.44815
Outer Radius of Be (cm)	0.25	0.25	0.25	0.45	0.45
DT cryo mass (mg)	0.6986	0.13	0.184	0.496	0.739
1_D Yield (MJ) for a 45 deg-half angle QSDD2	95	13	10.6	22.6	29.3
Percent Burn (%)	44	30.7	18	13.65	12.3
Max Ti(Kev)	48	43	21	19.5	18.3
Total rho-r (g/cm^2)	1.3			1.33	1.09
DT rho-r (g/cm^2)	0.777	0.186	0.23	0.32	0.397
DT-gas rho-r (g/cm^2)	0.05			0.1	0.104
Convergence Ratio of outer DT cryo radius	17	21	19.6	20.3	18.56
Maximum implosion velocity of Cryo_DT-Pusher interface (cm/microsecond)	-16	-22	-20	-26.8	-28
Minimum adiabat (alpha) at maximum implosion velocity	2.75	15	13	46	23.2
Fraction of DT mass on an adiabat > 1.5 times the minimum alpha	60	>50	>50	>50	60
Peter Amendt's Tau factor--(t_burn-t_freefall)/fwhm_burn_width)	-0.022	1.55	0.71	0.31	0.29
% Clean DT based on integration of David Youngs' criterion for mixed fuel--second integral of 0.14 of cryo interface decelertion.	81	46	55	67	75
Current in Be at 5 ns before burn (MA)	27	24	24	22	22
Current in Cryo DT at 5 ns before burn (MA)	5.7	5.5	5	8	7.8
Current in Gold at 5 ns before burn (MA)	7.4	0.6	1.2	4.6	5.3
Current in Gas DT at 5 ns before burn (MA)	0.66	1.2	1.26	1.9	1.8
Pressure from first shock (MB)	6.2	0.55	0.4	0.44	0.85
Burn width (Yield divided by Max burn rate) (ns)	1.2	0.226	0.396	0.45	0.363

Table 10: Results from 1-D LASNEX simulations of high-adiabat QSDD2 capsules

V. SUMMARY

A double shell quasi-spherical system designed to be driven by ZR at 28 MA has been simulated in 2D to give a simulated yield of 12 MJ from the ignition of the DT in the inner shell. The system on ZR has essentially no margin but a simulation of a double shell system scaled to a 56 MA driver has given a 130 MJ yield with considerable margin. We believe it will be very difficult to ignite the outer shell of a double shell system. For this reason we have modeled single shell systems with faster current rise times that are possible with MICA. SCREAMER simulations of MICA show that it should be possible to improve the 120 ns rise time, 28 MA current of ZR to a 30 ns rise time with 38 MA of current. 1D LASNEX simulations of implosions of single quasi-spherical beryllium shells filled with a layer of cryogenic DT show that ZR with MICA can give yields of over 100 MJ with convergence of 18. The 1D simulations also reveal that pure beryllium shells are preferable to beryllium shells with a layer of gold on the inside because the gold in the latter design expands early in the pulse and that leads to excessive entropy in the cryogenic DT. 2D simulations of these single shells will be addressed in a subsequent LDRD. 2D MACH2 simulations and QSDD1 LASNEX 2D simulations indicate that the long-wavelength RT instability does not destroy the symmetry of the implosion for the low-adiabat capsules examined with the 1-D LASNEX simulations. However, the MACH2 simulations show a bubble along the glide plane on the inside of the shell runs ahead of the rest of the shell implosion and leads to a detrimental "pancake" shape of the final DT. The MACH2 simulations show that a scraper along the glide plane can remove this bubble. The LASNEX simulations show that the bubble may be suppressed using a double shell system and a layer of shaped tuning foam.

VI. REFERENCES

1. R. Kirkpatrick, I. Lindemuth, M. Ward, Fusion Technology, **27**, 201, (1995)
2. J. Degnan, F. Lehr, J. Beason, *et al*, Phys. Rev. Lett. **74**, 98, (1995)
3. S. Slutz, R. Spielman, W. Stygar, *et al.*, See National Technical Information Service Document No. DE00003322, (Z-pinch driven isentropic compression for inertial fusion, Sandia National Laboratories report SAND98-2269), may be ordered from the National Technical Information Service, Springfield, VA, 22161
4. J. Hammer, J. Eddleman, P. Springer, Phys. Plasmas, **3**, 2063, (1996)
5. J. Lindl, Phys. Plasmas, **2**, 3933, (1995)
6. J.E. Bailey, G.A. Chandler, and S. Slutz, Phys. Rev. Lett. **92**, 085002 (2004)
7. T.J. Nash, D.H. McDaniel, R.J. Leeper, *et al*., Phys. Plasmas, **12**, 052705 (2005)
8. T. Nash, See National Technical Information Service Document No. DE2001-771501, (Adiabatic quasi-spherical compressions driven by magnetic pressure for inertial confinement fusion, Sandia National Laboratories report SAND2000-2654, November, 2000), may be ordered from the National Technical Information Service, Springfield, VA, 22161
9. Pace VanDevender and Norm Roderick for QSDD2, unpublished, October 2005.
10. W. A. Stygar, et al, Phys. Rev E **72**, 026404 (2005)
11. VanDevender, J. Appl. Phys, **50** (6), June 1979, pp 3928 to 3934
12. VanDevender, J. "Self-Magnetically Insulated Power Flow", Proceedings of 2nd International IEEE Pulsed Power Conference, Lubbock Texas, June 12-14, 1979
13. J. P. VanDevender, J. T. Crow, B. G. Epstein, D. H. McDaniel, C. W. Mendel, Jr., E. L. Neau, J. W. Poukey, J. P. Quintenz, D. B. Seidel, and R. W. Stinnett, Physica **104C**, (1981) p. 167-182
14. C. W. Mendel, Jr, and W. E. Rosenthal, Modeling magnetically insulated devices using flow impedance, Physics of Plasmas 2, **4** 1332-1342 (1995)
15. W. A. Stygar, H. C. Ives, D. L. Fehl, M.E. Cuneo, M. G. Mazarakis, J. E. Bailey, G. R. Bennett, D. E. Bliss, G. A. Chandler, R. J. Leeper, M. K. Matzen, D. H. McDaniel, J. S. McGurn, J. L. McKenney, L. P. Mix, D. J. Muron, J. L. Porter, J. J. Ramirez, L. E. Ruggles, J. F. Seamen, W. W. Simpson, c. S. Speas, R. B. Spielman, K. W. Struve, J. A. Torres, R. A. Vessey, T. C. Wagoner, T. L. Gililand, M. L. Horry, D. O. Jobe, S. E. Lazier, J. A. Mills, T. D. Mulville, J. H. Pyle, T. M. Romero, J. J. Seamen, and R.M. Smelser, Phys. Rev. E **69**, 046403 (2004)
16. Marcus Knudson, Sandia National Laboratories, Albuquerque, NM, personal correspondence, (2006).
17. Mattsson, AE; Schultz, PA; Desjarlais, MP; Mattsson, TR; Leung, K, "Designing meaningful density functional theory calculations in materials science - A primer" Modeling and Simulation in Materials Science and Engineering, **13**, no.1, p. R1-31, Jan., 2005
18. M. P. Desjarlais, Sandia National Laboratories, unpublished.
19. T.W. Hussey, N.F. Roderick and D.A. Kloc, "Scaling of (MHD) Instabilities in Imploding Plasma Liners," J. Appl. Phys., 51 (3) 1452, Mar 1980.

20. M. C. Herrmann, M. Tabak, and J. D. Lindl ˏ "A generalized scaling law for the ignition energy of inertial confinement fusion capsules." Nuclear Fusion, **41**, 1, pp. 99-111 (2001)
21. D. L. Youngs, "Modeling turbulent mixing by Rayleigh-Taylor Instability" Physica D **37**, no.1-3, p. 270-87 (July 1989)
22. Peter Amendt, H. F. Robey, H.-S. Park, R. E. Tipton, R. E. Turner, J. L Milovich, M. Bono, R. Hibbard, H. Louis, R. Wallace, and V. Yu. Glebov, "Holhraum-driven ignition-like double-shell implosion experiments on OMEGA" Phys Rev Lett **94**, 065004 (2005)
23. R.E. Peterkin Jr., M.H. Frese, and C.R. Sovinec, "Transport of magnetic flux in an arbitrary coordinate ALE code," J. Comp. Phys., **140**, pp.148-171, 1998.
24. J. P. VanDevender and N. F. Roderick, "Quasi-Spherical Current Driven ICF," Presentation at Sandia National Laboratories, November 2005.
25. J.H. Hammer, M. Tabak, S.C. Wilks, J.D. Lindl, D.S. Bailey, P/W. Rambo, A. Toor, G.B. Zimmerman, J.L. Porter, "High yield inertial confinement fusion target design for a z-pinch-driven hohlraum," Physics of Plasmas, **6**, no.5, pt.2, p.2129-2136, May, 1999

Appendix A. SCREAMER deck for MICA part a

MICA-Magnetically Insulated Current Amplifier version 6
!Voltage Source is time-jittered version distributed by Ken Struve through Mike Cuneo Sept 2006
!Inductance of can is corrected from version 5. to be 0.66 nH for 9 lines or 0.22 nH for 27 lines for 30 deg capsules.
!MICAs from spiral MITL have convolutes and QSDD2 loads
!ZoMITL=0.239 Ohms, ZMICA =0.64 Zo,MITL from William Langston 3-D Quicksilver simulations
! Zflow=0.79 Zo.min in convolute from MITE Type II Convolute Data
!Capsule is for ZR with theta = 60 deg, 2.5 mm radius and 8.48 mg mass with 0.192 mg of DT
!MICA1, 2 and 3 switch at 174 ns
!For each MICA mass/length is 0.333xTotal Mass and lenght is 3 times total length
!For each of 3 MICA Capsules SPH 0.0025 134. 2.83E-6 .0001 for baseline 0.2 Hammer Mass Target
!10.0 m spiral MITL
!Resistive Wall Losses Included
!ZR at 2Vo=10.0 MV, from Table
!Rs=0.179 Ohms, and Lv=7.02 nH
!MITL is zo=.239 Ohms and 33.3 ns (10m)long
!MITL is divided into 6.667, 13.333, 13.333 ns segments
!Extra 250 ns TRL after VOLTSOURCE is removed; runs show no difference except tswitch
!Endbranches of switch and MITL comes off nodes between MITL Segments and at end
!Separate file adds currents to common load
!MICA gaps are 3mm to 2 mm and Disk Feed Gap is 2 mm to 1 mm with minimum Z0 = 1.0 Ohms
!MICA and Disk Inductances calculated for triangular X-section lines
!Vary gaps by factor M by multiplying MICA TRL impedances and Zflow and Disk Induct. by M
!Each of 27 switches has its own line to disk
!Current sources are recorded and added as MICAs in separate calculation (B)
TIME-STEP 2.0E-11
RESOLUTION-TIME 1.0E-10
END-TIME 3.E-7
NUMBER-PRINTS 1
EXECUTE-CYCLES ALL
ECHO NO
MAX-POINTS 3000
!
!
! Pace VanDevender
!
BRANCH
!
VOLTSOURCE TAB 0.179 0.0

```
1.0 0.0
0        190000
2.00E-09     197000
3.00E-09     202000
5.00E-09     206000
6.00E-09     209000
8.00E-09     212000
1.00E-08     213000
1.10E-08     214000
1.30E-08     214000
1.40E-08     214000
1.60E-08     214000
1.80E-08     215000
1.90E-08     220000
2.10E-08     229000
2.20E-08     245000
2.40E-08     270000
2.60E-08     303000
2.70E-08     344000
2.90E-08     391000
3.00E-08     447000
3.20E-08     511000
3.40E-08     585000
3.50E-08     669000
3.70E-08     768000
3.80E-08     8.77E+05
4.00E-08     9.95E+05
4.20E-08     1.12E+06
4.30E-08     1.25E+06
4.50E-08     1.38E+06
4.60E-08     1.53E+06
4.80E-08     1.70E+06
5.00E-08     1.90E+06
5.10E-08     2.17E+06
5.30E-08     2.45E+06
5.40E-08     2.73E+06
5.60E-08     3.03E+06
5.80E-08     3.39E+06
5.90E-08     3.75E+06
6.10E-08     4.06E+06
6.20E-08     4.33E+06
6.40E-08     4610000
6.60E-08     4890000
6.70E-08     5120000
6.90E-08     5300000
7.00E-08     5460000
7.20E-08     5620000
7.40E-08     5750000
```

7.50E-08	5850000
7.70E-08	5930000
7.80E-08	6020000
8.00E-08	6110000
8.20E-08	6190000
8.30E-08	6280000
8.50E-08	6390000
8.60E-08	6490000
8.80E-08	6620000
9.00E-08	6750000
9.10E-08	6890000
9.30E-08	7020000
9.40E-08	7150000
9.60E-08	7290000
9.80E-08	7420000
9.90E-08	7540000
1.01E-07	7670000
1.02E-07	7790000
1.04E-07	7910000
1.06E-07	8030000
1.07E-07	8140000
1.09E-07	8260000
1.10E-07	8380000
1.12E-07	8490000
1.14E-07	8600000
1.15E-07	8720000
1.17E-07	8840000
1.18E-07	8960000
1.20E-07	9070000
1.22E-07	9190000
1.23E-07	9290000
1.25E-07	9390000
1.26E-07	9450000
1.28E-07	9500000
1.30E-07	9510000
1.31E-07	9500000
1.33E-07	9.47E+06
1.34E-07	9.41E+06
1.36E-07	9.32E+06
1.38E-07	9.22E+06
1.39E-07	9.10E+06
1.41E-07	8.97E+06
1.42E-07	8.85E+06
1.44E-07	8.73E+06
1.46E-07	8.61E+06
1.47E-07	8.50E+06
1.49E-07	8.39E+06
1.50E-07	8.29E+06

1.52E-07	8.19E+06
1.54E-07	8.10E+06
1.55E-07	8.00E+06
1.57E-07	7.91E+06
1.58E-07	7.82E+06
1.60E-07	7.72E+06
1.62E-07	7.62E+06
1.63E-07	7.53E+06
1.65E-07	7.44E+06
1.66E-07	7.36E+06
1.68E-07	7.29E+06
1.70E-07	7.23E+06
1.71E-07	7.19E+06
1.73E-07	7.17E+06
1.74E-07	7.15E+06
1.76E-07	7.13E+06
1.78E-07	7.12E+06
1.79E-07	7.09E+06
1.81E-07	7.06E+06
1.82E-07	7.02E+06
1.84E-07	6.96E+06
1.86E-07	6.89E+06
1.87E-07	6.81E+06
1.89E-07	6.72E+06
1.90E-07	6.63E+06
1.92E-07	6.53E+06
1.94E-07	6.42E+06
1.95E-07	6.33E+06
1.97E-07	6.24E+06
1.98E-07	6.16E+06
2.00E-07	6.08E+06
2.02E-07	6.02E+06
2.03E-07	5.96E+06
2.05E-07	5.92E+06
2.06E-07	5.87E+06
2.08E-07	5.83E+06
2.10E-07	5.80E+06
2.11E-07	5.76E+06
2.13E-07	5.73E+06
2.14E-07	5.69E+06
2.16E-07	5.65E+06
2.18E-07	5.61E+06
2.19E-07	5.56E+06
2.21E-07	5.52E+06
2.22E-07	5.47E+06
2.24E-07	5.43E+06
2.26E-07	5.40E+06
2.27E-07	5.37E+06

2.29E-07	5.35E+06
2.30E-07	5.33E+06
2.32E-07	5.31E+06
2.34E-07	5.29E+06
2.35E-07	5.28E+06
2.37E-07	5.27E+06
2.38E-07	5.25E+06
2.40E-07	5.24E+06
2.42E-07	5.23E+06
2.43E-07	5.21E+06
2.45E-07	5.20E+06
2.46E-07	5.18E+06
2.48E-07	5.15E+06
2.50E-07	5.11E+06
2.51E-07	5.08E+06
2.53E-07	5.03E+06
2.54E-07	4.98E+06
2.56E-07	4.91E+06
2.58E-07	4.84E+06
2.59E-07	4.76E+06
2.61E-07	4.67E+06
2.62E-07	4.58E+06
2.64E-07	4.48E+06
2.66E-07	4.39E+06
2.67E-07	4.30E+06
2.69E-07	4.21E+06
2.70E-07	4.13E+06
2.72E-07	4.05E+06
2.74E-07	3.98E+06
2.75E-07	3.92E+06
2.77E-07	3.86E+06
2.78E-07	3.82E+06
2.80E-07	3.78E+06
2.82E-07	3.75E+06
2.83E-07	3.72E+06
2.85E-07	3.70E+06
2.86E-07	3.68E+06
2.88E-07	3.66E+06
2.90E-07	3.65E+06
2.91E-07	3.63E+06
2.93E-07	3.61E+06
2.94E-07	3.59E+06
2.96E-07	3.58E+06
2.98E-07	3.56E+06
2.99E-07	3.54E+06
3.01E-07	3.53E+06
3.02E-07	3.51E+06
3.04E-07	3.49E+06

3.06E-07	3.47E+06
3.07E-07	3.44E+06
3.09E-07	3.41E+06
3.10E-07	3.38E+06
3.12E-07	3.35E+06
3.14E-07	3.32E+06
3.15E-07	3.29E+06
3.17E-07	3.26E+06
3.18E-07	3.24E+06
3.20E-07	3.22E+06
3.22E-07	3.21E+06
3.23E-07	3.20E+06
3.25E-07	3.19E+06
3.26E-07	3.19E+06
3.28E-07	3.18E+06
3.30E-07	3.17E+06
3.31E-07	3.17E+06
3.33E-07	3.16E+06
3.34E-07	3.15E+06
3.36E-07	3.14E+06
3.38E-07	3.13E+06
3.39E-07	3.12E+06
3.41E-07	3.11E+06
3.42E-07	3.10E+06
3.44E-07	3.09E+06
3.46E-07	3.07E+06
3.47E-07	3.06E+06
3.49E-07	3.04E+06
3.50E-07	3.02E+06
3.52E-07	3.00E+06
3.54E-07	2.98E+06
3.55E-07	2.96E+06
3.57E-07	2.94E+06
3.58E-07	2.92E+06
3.60E-07	2.91E+06
3.62E-07	2.90E+06
3.63E-07	2.89E+06
3.65E-07	2.88E+06
3.66E-07	2.87E+06
3.68E-07	2.85E+06
3.70E-07	2.83E+06
3.71E-07	2.81E+06
3.73E-07	2.78E+06
3.74E-07	2.75E+06
3.76E-07	2.71E+06
3.78E-07	2.67E+06
3.79E-07	2.63E+06
3.81E-07	2.59E+06

3.82E-07	2.56E+06
3.84E-07	2.52E+06
3.86E-07	2.47E+06
3.87E-07	2.43E+06
3.89E-07	2.39E+06
3.90E-07	2.35E+06
3.92E-07	2.31E+06
3.94E-07	2.26E+06
3.95E-07	2.22E+06
3.97E-07	2.18E+06
3.98E-07	2.13E+06
4.00E-07	2.09E+06
4.02E-07	2.04E+06
4.03E-07	2.00E+06
4.05E-07	1.96E+06
4.06E-07	1.92E+06
4.08E-07	1.88E+06
4.10E-07	1.84E+06
4.11E-07	1.81E+06
4.13E-07	1.78E+06
4.14E-07	1.74E+06
4.16E-07	1.71E+06
4.18E-07	1.67E+06
4.19E-07	1.63E+06
4.21E-07	1.59E+06
4.22E-07	1.54E+06
4.24E-07	1.48E+06
4.26E-07	1.42E+06
4.27E-07	1.35E+06
4.29E-07	1.28E+06
4.30E-07	1.21E+06
4.32E-07	1.13E+06
4.34E-07	1.06E+06
4.35E-07	9.80E+05
4.37E-07	9.04E+05
4.38E-07	8.28E+05
4.40E-07	7.50E+05
4.42E-07	6.71E+05
4.43E-07	5.90E+05
4.45E-07	5.08E+05
4.46E-07	4.29E+05
4.48E-07	3.51E+05
4.50E-07	2.77E+05
4.51E-07	2.06E+05
4.53E-07	1.36E+05
4.54E-07	6.95E+04
4.56E-07	5.58E+03
4.58E-07	0.00E+00

```
1.25E-06      0.00E+00
LAST-ENTRY
!
!
TRL Lin 34e-9 0.2
CSV Vin
$VIN2
CSV Iin
$IIN2
TRL Lin 14e-9 0.29
TRL Lin 8e-9 0.37
CSV VOUT
$VMitl_in
CSV IOUT
$IMitl_in
RLS 0.0 3.13E-9  !Vacuum insulator inductance including vac flare.
!
!
!27.6 m circumference, 0.0175 m gap, 33 ns transit time
!0.239 Ohm impedance and divided into 6.7, 13.3, 13.3 ns segments
MITL 27.6 0.0175 6.67E-9 0.239
CSV VOUT
$VatMICA1
RCG 1.E6 0.0
ENDBRANCH !MICA1
MITL 27.6 0.0175 13.33E-9 0.239
CSV VOUT
$VatMICA2
RCG 1.E6 0.0
ENDBRANCH !MICA2
MITL 27.6 0.0175 13.33E-9 0.239
CSV VOUT
$VatMICA3
!
CSV IIN
$IMITL3IN
CSV IOUT
$IMITL3OUT
!
RCG 1.E6 0.0
ENDBRANCH !MICA3
!Isolate output from MITL
RLS 1.E6 0.0
!
RLS1 0.001 0.1E-9
RCG 1.E6 0.0
!
```

!
===
===
! E N D O F MAIN BRANCH
!
===
===
!***MICA1**********
BRANCH !MICA1
PISECTION 1.E4 0. 1.E6 0.0 1.E4 0.   !Lswitch =1.0 nH for 2 cm long SW and 9
lines
VARIABLE R2 EXP-MODEL
1.E6 1.E-3 1.74E-7 1.E-9 0.36
RCG 1.E6 0.0
CSV VR1
$VMICA1
RLS 1.E-6 1.E-9   !Switch Inductance
CSV IR2
$IMICA1
!
TRL LIN 0.3E-9 2.0 0.8 1.E-10
TRL LIN 0.75E-9 0.8 1.0 1.E-10   !**********************************
TRL LIN 2.0E-9 1.0 1.0 1.E-10   !**********************************
!
!Zflow=0.79*Zo,min from MITE Data   ****************************
RCG 0.0001 0.1e-09
VARIABLE R1 POS-MODEL
! TSW CURSW TOPEN ZFLOW GSWMIN GSWMAX CBFLAG
0.0 1.0E2 0. 0.8 .00001 10000 0.0
CSV IIN
$ZFLOWIIn1
CSV IOUT
$ZFLOWIOUT1
!
!
TRL LIN 1.0E-9 1.0 1.4 1.E-10   !***************************************
RLS 0.0 2.71e-9   !Disk Feed inductance = 2.71 nH
!
!
! ** ACTIVE FOIL LOAD, ro LENGTH mass rmin
!CYLFOIL 2.0E-2 2.0E-2 9.4E-6 2.0E-3
RLS 0. 0.66E-9   !Can Inductance
!CYLFOIL 1.E-2 6.0E-2 1.33E-6 1.E-3
!SPH 0.0025 166. 2.32E-6 .0001
SPH 0.0025 134. 2.83E-6 .0001
!rinit in m, full angle in degrees, mass in kg, rfinal in m
CSV L2
$ LMICA1

CSV VL2
$VLMICA1
CSV IL2
$ ILMICA1
RCG 0.0 0.0
!
!***MICA2**********
BRANCH ! !MICA2
PISECTION 1.E4 0. 1.E6 0.0 1.E4 0.   !Lswitch =1.0 nH for 2 cm long SW and 9
lines
VARIABLE R2 EXP-MODEL
1.E6 1.E-3 1.74E-7 1.E-9 0.36
RCG 1.E6 0.0
CSV VR1
$VMICA2
RLS 1.E-6 1.E-9
CSV IR2
$IMICA2
!
TRL LIN 0.23E-9 2.0 0.8 1.E-10
TRL LIN 0.65E-9 0.8 1.0 1.E-10
TRL LIN 1.5E-9 1.0 1.0 1.E-10
!
!Zflow=0.79*Zo,min from MITE Data   ******************************
RCG 0.0001 0.1e-09
VARIABLE R1 POS-MODEL
! TSW CURSW TOPEN ZFLOW GSWMIN GSWMAX CBFLAG
0.0 1.0E2 0. 0.8 .00001 10000 0.0
CSV IIN
$ZFLOWIIn2
CSV IOUT
$ZFLOWIOUT2
!
TRL LIN 0.7E-9 1.0 1.4 1.E-10   !***************************************
RLS 0.0 2.71e-9   !Disk Feed inductance = 2.71 nH
!
! ** ACTIVE FOIL LOAD, ro LENGTH mass rmin
!CYLFOIL 2.0E-2 2.0E-2 9.4E-6 2.0E-3
RLS 0. 0.66E-9   !Can Inductance
!CYLFOIL 1.E-2 6.0E-2 1.33E-6 1.E-3
SPH 0.0025 134. 2.83E-6 .0001
!rinit in m, full angle in degrees, mass in kg, rfinal in m
CSV L2
$ LMICA2
CSV VL2
$VLMICA2
CSV IL2
$ ILMICA2

RCG 0.0 0.0
!
!***MICA3**********
BRANCH !MICA3
PISECTION 1.E4 0. 1.E6 0.0 1.E4 0.   !Lswitch =1.0 nH for 2 cm long SW and 9
lines
VARIABLE R2 EXP-MODEL
1.E6 1.E-3 1.74E-7 5.E-10 0.36
RCG 1.E6 0.0
CSV VR1
$VMICA3
RLS 1.E-6 1.E-9   !Switch Inductance
CSV IR2
$IMICA3
!
TRL LIN 0.1E-9 2.0 1.0 1.E-10
TRL LIN 0.14E-9 1.0 1.0 1.E-10   !*************************************
TRL LIN 0.9E-9 1.0 1.0 1.E-10   !*************************************
!
!Zflow=0.79*Zo,min from MITE Data   *****************************
RCG 0.0001 0.1e-09
VARIABLE R1 POS-MODEL
! TSW CURSW TOPEN ZFLOW GSWMIN GSWMAX CBFLAG
0.0 1.0E2 0. 0.8 .00001 10000 0.0
CSV IIN
$ZFLOWIIn3
CSV IOUT
$ZFLOWIOUT3
!
TRL LIN 0.69E-9 1.0 1.4 1.E-10   !*************************************
RLS 0.0 2.71e-9   !Disk Feed inductance = 2.71e-9
!
!
! ** ACTIVE FOIL LOAD, ro LENGTH mass rmin
!CYLFOIL 2.0E-2 2.0E-2 9.4E-6 2.0E-3
RLS 0. 0.66E-9   !Can Inductance
!CYLFOIL 1.E-2 6.0E-2 1.33E-6 1.E-3
!SPH 0.0025 166. 2.32E-6 .0001
SPH 0.0025 134. 2.83E-6 .0001
!rinit in m, full angle in degrees, mass in kg, rfinal in m
CSV L2
$ LMICA3
CSV VL2
$VLMICA3
CSV IL2
$ ILMICA3
RCG 0.0 0.0
!

!
!
!
==
===
! E N D O F S I M U L A T I O N
!
==
===

Appendix B SCREAMER deck for MICA part b

MICA-Magnetically Insulated Current Amplifier version 6
!Voltage Source is time-jittered version distributed by Ken Struve through Mike Cuneo Sept 2006
!Inductance of can is corrected from version 5. to be 0.66 nH for 9 lines or 0.22 nH for 27 lines for 30 deg capsules.
!MICAs from spiral MITL have convolutes and QSDD2 loads
!ZoMITL=0.239 Ohms, ZMICA =0.64 Zo,MITL from William Langston 3-D Quicksilver simulations
! Zflow=0.79 Zo.min in convolute from MITE Type II Convolute Data
!Capsule is for ZR with theta = 60 deg, 2.5 mm radius and 8.48 mg mass
!MICA1, 2 and 3 switch at 174 ns
!For each MICA mass/length is 0.333xTotal Mass and lenght is 3 times total length
!For each of 3 MICA Capsules SPH 0.0025 134. 2.83E-6 .0001 for baseline 0.2 Hammer Mass Target
!10.0 m spiral MITL
!Resistive Wall Losses Included
!ZR at 2Vo=10.0 MV, from Table
!Rs=0.179 Ohms, and Lv=7.02 nH
!MITL is zo=.239 Ohms and 33.3 ns (10m)long
!MITL is divided into 6.667, 13.333, 13.333 ns segments
!Extra 250 ns TRL after VOLTSOURCE is removed; runs show no difference except tswitch
!Endbranches of switch and MITL comes off nodes between MITL Segments and at end
!Separate file adds currents to common load
!MICA gaps are 3mm to 2 mm and Disk Feed Gap is 2 mm to 1 mm with minimum Z0 = 1.0 Ohms
!MICA and Disk Inductances calculated for triangular X-section lines
!Vary gaps by factor M by multiplying MICA TRL impedances and Zflow and Disk Induct. by M
!Each of 27 switches has its own line to disk
!Current sources are recorded and added as MICAs in separate calculation (B)--This File.
TIME-STEP 2.0E-11
RESOLUTION-TIME 1.0E-10
END-TIME 3.E-7
NUMBER-PRINTS 1
EXECUTE-CYCLES ALL
ECHO NO
MAX-POINTS 3000
!
!
! Pace VanDevender
!
BRANCH
!Voltage Source is time-jittered version distributed by Ken Struve through Mike Cuneo Sept 2006
VOLTSOURCE TAB 0.179 0.0

```
1.0 0.0
0        190000
2.00E-09      197000
3.00E-09      202000
5.00E-09      206000
6.00E-09      209000
8.00E-09      212000
1.00E-08      213000
1.10E-08      214000
1.30E-08      214000
1.40E-08      214000
1.60E-08      214000
1.80E-08      215000
1.90E-08      220000
2.10E-08      229000
2.20E-08      245000
2.40E-08      270000
2.60E-08      303000
2.70E-08      344000
2.90E-08      391000
3.00E-08      447000
3.20E-08      511000
3.40E-08      585000
3.50E-08      669000
3.70E-08      768000
3.80E-08      8.77E+05
4.00E-08      9.95E+05
4.20E-08      1.12E+06
4.30E-08      1.25E+06
4.50E-08      1.38E+06
4.60E-08      1.53E+06
4.80E-08      1.70E+06
5.00E-08      1.90E+06
5.10E-08      2.17E+06
5.30E-08      2.45E+06
5.40E-08      2.73E+06
5.60E-08      3.03E+06
5.80E-08      3.39E+06
5.90E-08      3.75E+06
6.10E-08      4.06E+06
6.20E-08      4.33E+06
6.40E-08      4610000
6.60E-08      4890000
6.70E-08      5120000
6.90E-08      5300000
7.00E-08      5460000
7.20E-08      5620000
7.40E-08      5750000
```

7.50E-08	5850000
7.70E-08	5930000
7.80E-08	6020000
8.00E-08	6110000
8.20E-08	6190000
8.30E-08	6280000
8.50E-08	6390000
8.60E-08	6490000
8.80E-08	6620000
9.00E-08	6750000
9.10E-08	6890000
9.30E-08	7020000
9.40E-08	7150000
9.60E-08	7290000
9.80E-08	7420000
9.90E-08	7540000
1.01E-07	7670000
1.02E-07	7790000
1.04E-07	7910000
1.06E-07	8030000
1.07E-07	8140000
1.09E-07	8260000
1.10E-07	8380000
1.12E-07	8490000
1.14E-07	8600000
1.15E-07	8720000
1.17E-07	8840000
1.18E-07	8960000
1.20E-07	9070000
1.22E-07	9190000
1.23E-07	9290000
1.25E-07	9390000
1.26E-07	9450000
1.28E-07	9500000
1.30E-07	9510000
1.31E-07	9500000
1.33E-07	9.47E+06
1.34E-07	9.41E+06
1.36E-07	9.32E+06
1.38E-07	9.22E+06
1.39E-07	9.10E+06
1.41E-07	8.97E+06
1.42E-07	8.85E+06
1.44E-07	8.73E+06
1.46E-07	8.61E+06
1.47E-07	8.50E+06
1.49E-07	8.39E+06
1.50E-07	8.29E+06

1.52E-07	8.19E+06
1.54E-07	8.10E+06
1.55E-07	8.00E+06
1.57E-07	7.91E+06
1.58E-07	7.82E+06
1.60E-07	7.72E+06
1.62E-07	7.62E+06
1.63E-07	7.53E+06
1.65E-07	7.44E+06
1.66E-07	7.36E+06
1.68E-07	7.29E+06
1.70E-07	7.23E+06
1.71E-07	7.19E+06
1.73E-07	7.17E+06
1.74E-07	7.15E+06
1.76E-07	7.13E+06
1.78E-07	7.12E+06
1.79E-07	7.09E+06
1.81E-07	7.06E+06
1.82E-07	7.02E+06
1.84E-07	6.96E+06
1.86E-07	6.89E+06
1.87E-07	6.81E+06
1.89E-07	6.72E+06
1.90E-07	6.63E+06
1.92E-07	6.53E+06
1.94E-07	6.42E+06
1.95E-07	6.33E+06
1.97E-07	6.24E+06
1.98E-07	6.16E+06
2.00E-07	6.08E+06
2.02E-07	6.02E+06
2.03E-07	5.96E+06
2.05E-07	5.92E+06
2.06E-07	5.87E+06
2.08E-07	5.83E+06
2.10E-07	5.80E+06
2.11E-07	5.76E+06
2.13E-07	5.73E+06
2.14E-07	5.69E+06
2.16E-07	5.65E+06
2.18E-07	5.61E+06
2.19E-07	5.56E+06
2.21E-07	5.52E+06
2.22E-07	5.47E+06
2.24E-07	5.43E+06
2.26E-07	5.40E+06
2.27E-07	5.37E+06

2.29E-07	5.35E+06
2.30E-07	5.33E+06
2.32E-07	5.31E+06
2.34E-07	5.29E+06
2.35E-07	5.28E+06
2.37E-07	5.27E+06
2.38E-07	5.25E+06
2.40E-07	5.24E+06
2.42E-07	5.23E+06
2.43E-07	5.21E+06
2.45E-07	5.20E+06
2.46E-07	5.18E+06
2.48E-07	5.15E+06
2.50E-07	5.11E+06
2.51E-07	5.08E+06
2.53E-07	5.03E+06
2.54E-07	4.98E+06
2.56E-07	4.91E+06
2.58E-07	4.84E+06
2.59E-07	4.76E+06
2.61E-07	4.67E+06
2.62E-07	4.58E+06
2.64E-07	4.48E+06
2.66E-07	4.39E+06
2.67E-07	4.30E+06
2.69E-07	4.21E+06
2.70E-07	4.13E+06
2.72E-07	4.05E+06
2.74E-07	3.98E+06
2.75E-07	3.92E+06
2.77E-07	3.86E+06
2.78E-07	3.82E+06
2.80E-07	3.78E+06
2.82E-07	3.75E+06
2.83E-07	3.72E+06
2.85E-07	3.70E+06
2.86E-07	3.68E+06
2.88E-07	3.66E+06
2.90E-07	3.65E+06
2.91E-07	3.63E+06
2.93E-07	3.61E+06
2.94E-07	3.59E+06
2.96E-07	3.58E+06
2.98E-07	3.56E+06
2.99E-07	3.54E+06
3.01E-07	3.53E+06
3.02E-07	3.51E+06
3.04E-07	3.49E+06

3.06E-07	3.47E+06
3.07E-07	3.44E+06
3.09E-07	3.41E+06
3.10E-07	3.38E+06
3.12E-07	3.35E+06
3.14E-07	3.32E+06
3.15E-07	3.29E+06
3.17E-07	3.26E+06
3.18E-07	3.24E+06
3.20E-07	3.22E+06
3.22E-07	3.21E+06
3.23E-07	3.20E+06
3.25E-07	3.19E+06
3.26E-07	3.19E+06
3.28E-07	3.18E+06
3.30E-07	3.17E+06
3.31E-07	3.17E+06
3.33E-07	3.16E+06
3.34E-07	3.15E+06
3.36E-07	3.14E+06
3.38E-07	3.13E+06
3.39E-07	3.12E+06
3.41E-07	3.11E+06
3.42E-07	3.10E+06
3.44E-07	3.09E+06
3.46E-07	3.07E+06
3.47E-07	3.06E+06
3.49E-07	3.04E+06
3.50E-07	3.02E+06
3.52E-07	3.00E+06
3.54E-07	2.98E+06
3.55E-07	2.96E+06
3.57E-07	2.94E+06
3.58E-07	2.92E+06
3.60E-07	2.91E+06
3.62E-07	2.90E+06
3.63E-07	2.89E+06
3.65E-07	2.88E+06
3.66E-07	2.87E+06
3.68E-07	2.85E+06
3.70E-07	2.83E+06
3.71E-07	2.81E+06
3.73E-07	2.78E+06
3.74E-07	2.75E+06
3.76E-07	2.71E+06
3.78E-07	2.67E+06
3.79E-07	2.63E+06
3.81E-07	2.59E+06

3.82E-07	2.56E+06
3.84E-07	2.52E+06
3.86E-07	2.47E+06
3.87E-07	2.43E+06
3.89E-07	2.39E+06
3.90E-07	2.35E+06
3.92E-07	2.31E+06
3.94E-07	2.26E+06
3.95E-07	2.22E+06
3.97E-07	2.18E+06
3.98E-07	2.13E+06
4.00E-07	2.09E+06
4.02E-07	2.04E+06
4.03E-07	2.00E+06
4.05E-07	1.96E+06
4.06E-07	1.92E+06
4.08E-07	1.88E+06
4.10E-07	1.84E+06
4.11E-07	1.81E+06
4.13E-07	1.78E+06
4.14E-07	1.74E+06
4.16E-07	1.71E+06
4.18E-07	1.67E+06
4.19E-07	1.63E+06
4.21E-07	1.59E+06
4.22E-07	1.54E+06
4.24E-07	1.48E+06
4.26E-07	1.42E+06
4.27E-07	1.35E+06
4.29E-07	1.28E+06
4.30E-07	1.21E+06
4.32E-07	1.13E+06
4.34E-07	1.06E+06
4.35E-07	9.80E+05
4.37E-07	9.04E+05
4.38E-07	8.28E+05
4.40E-07	7.50E+05
4.42E-07	6.71E+05
4.43E-07	5.90E+05
4.45E-07	5.08E+05
4.46E-07	4.29E+05
4.48E-07	3.51E+05
4.50E-07	2.77E+05
4.51E-07	2.06E+05
4.53E-07	1.36E+05
4.54E-07	6.95E+04
4.56E-07	5.58E+03
4.58E-07	0.00E+00

```
1.25E-06      0.00E+00
LAST-ENTRY
!
!
TRL Lin 34e-9 0.2
CSV Vin
$VIN2
CSV Iin
$IIN2
TRL Lin 14e-9 0.29
TRL Lin 8e-9 0.37
CSV VOUT
$VMitl_in
CSV IOUT
$IMitl_in
RLS 0.0 3.13E-9  !Vacuum insulator inductance including vac flare.
!
!
!27.6 m circumference, 0.0175 m gap, 33 ns transit time
!0.239 Ohm impedance and divided into 6.7, 13.3, 13.3 ns segments
MITL 27.6 0.0175 6.67E-9 0.239
CSV VOUT
$VatMICA1
RCG 1.E6 0.0
ENDBRANCH !MICA1
MITL 27.6 0.0175 13.33E-9 0.239
CSV VOUT
$VatMICA2
RCG 1.E6 0.0
ENDBRANCH !MICA2
MITL 27.6 0.0175 13.33E-9 0.239
CSV VOUT
$VatMICA3
!
CSV IIN
$IMITL3IN
CSV IOUT
$IMITL3OUT
!
RCG 1.E6 0.0
PISECTION 1.E4 0. 1.E6 0.0 1.E4 0.           !Lswitch =1.0 nH for 2 cm long SW and 9
lines
VARIABLE R2 EXP-MODEL
1.E6 1.E-3 1.74E-7 5.E-10 0.36        !************Enter Switch Timing**********
RCG 1.E6 0.0
CSV VR1
$VMICA3
RLS 1.E-6 1.E-9
```

CSV IR2
$IMICA3
!
TRL LIN 0.1E-9 2.0 1.0 1.E-10
TRL LIN 0.14E-9 1.0 1.0 1.E-10   !*****************************
TRL LIN 0.9E-9 1.0 1.0 1.E-10   !*****************************
Endbranch !Attach MICA1
!
RLS1 0.001 0.0
RCG 1.E6 0.0
Endbranch !Attach MICA2
!
!Zflow=0.79*Zo,min from MITE Data with Zo,min =the three Zo.min in parallel
RCG 0.0001 0.0   !ZFLOW Losses for all three MICAs
VARIABLE R1 POS-MODEL
! TSW CURSW TOPEN ZFLOW GSWMIN GSWMAX CBFLAG
      ****
0.0 1.0E2 0. 0.333 .00001 10000 0.0
CSV IIN
$ZFLOWIIn1
CSV IOUT
$ZFLOWIOUT1
!
TRL LIN 0.8E-9 0.333 0.47 1.E-10   !Last stage of MICA Inductances--averaged for
common MICA line **
!
RLS 0.001 0.0
RCG 1.E6 0.0
CSV VR2
$VbeforeRWLOSSES!
!
RLS 0.0 0.0
VAR R2 RWALL_MODEL
!tstart const disk1inner disk1outer disk2inner disk2outer
4.31E-7 0.0 0.00259 0.08 0.00259 0.08
0.00259 0.00259 0.08 0.001
CSV VR2
$VRESWALLLOSS
CSV IR2
$IRESWALLLOSS
CSV ER2
$EnergyRESWALLLOSS
!
RCG 1.E6 0.0
CSV VR1
$VMICAs
RLS 1.E-4 0.0
CSV IR2

$VMICAs
!
RLS 0.0 0.9e-9   !Disk Feed inductance = 0.9 nH
!
!
RLS 0. 0.22E-9   !Can Inductance
SPH 0.0025 60. 8.48E-6 .0001
!rinit in m, full angle in degrees, mass in kg, rfinal in m
CSV L2
$ LLOAD
CSV VL2
$VLOAD
CSV IL2
$ ILOAD
CSV PIN
$PLOAD
CSV EIN
$ELOAD
!
RCG 0.0001 0
!
!
==
===
! E N D O F MAIN BRANCH
!
==
===
!***MICA1**********
BRANCH !MICA1
PISECTION 1.E4 0. 1.E6 0.0 1.E4 0.   !Lswitch =1.0 nH for 2 cm long SW and 9
lines
VARIABLE R2 EXP-MODEL
1.E6 1.E-3 1.74E-7 1.E-9 0.36
RCG 1.E6 0.0
CSV VR1
$VMICA1
RLS 1.E-6 1.E-9   !Switch Inductance
CSV IR2
$IMICA1
!
TRL LIN 0.3E-9 2.0 0.8 1.E-10
TRL LIN 0.75E-9 0.8 1.0 1.E-10   !********************************
TRL LIN 2.0E-9 1.0 1.0 1.E-10   !********************************
!
!Zflow=0.79*Zo,min from MITE Data   ******************************
RCG 0.0001 0.1e-09
VARIABLE R1 POS-MODEL

```
! TSW CURSW TOPEN ZFLOW GSWMIN GSWMAX CBFLAG
0.0 1.0E2 0. 0.8 .00001 10000 0.0
CSV IIN
$ZFLOWIIn1
CSV IOUT
$ZFLOWIOUT1
!
!
TRL LIN 1.0E-9 1.0 1.4 1.E-10        !****************************************
RLS 0.0 2.71e-9        !Disk Feed inductance = 2.71 nH
!
!
! ** ACTIVE FOIL LOAD, ro LENGTH mass rmin
!CYLFOIL 2.0E-2 2.0E-2 9.4E-6 2.0E-3
RLS 0. 0.66E-9        !Can Inductance
!CYLFOIL 1.E-2 6.0E-2 1.33E-6 1.E-3
!SPH 0.0025 166. 2.32E-6 .0001
SPH 0.0025 134. 2.83E-6 .0001
!rinit in m, full angle in degrees, mass in kg, rfinal in m
CSV L2
$ LMICA1
CSV VL2
$VLMICA1
CSV IL2
$ ILMICA1
RCG 0.0 0.0
!
!*************************************************MICA2**********
BRANCH ! !MICA2
PISECTION 1.E4 0. 1.E6 0.0 1.E4 0.        !Lswitch =1.0 nH for 2 cm long SW and 9
lines
VARIABLE R2 EXP-MODEL
1.E6 1.E-3 1.74E-7 1.E-9 0.36
RCG 1.E6 0.0
CSV VR1
$VMICA2
RLS 1.E-6 1.E-9
CSV IR2
$IMICA2
!
TRL LIN 0.23E-9 2.0 0.8 1.E-10
TRL LIN 0.65E-9 0.8 1.0 1.E-10
TRL LIN 1.5E-9 1.0 1.0 1.E-10
!
!Zflow=0.79*Zo,min from MITE Data        *****************************
RCG 0.0001 0.1e-09
VARIABLE R1 POS-MODEL
! TSW CURSW TOPEN ZFLOW GSWMIN GSWMAX CBFLAG
```

```
0.0 1.0E2 0. 0.8 .00001 10000 0.0
CSV IIN
$ZFLOWIIn2
CSV IOUT
$ZFLOWIOUT2
!
TRL LIN 0.7E-9 1.0 1.4 1.E-10          !*************************************
RLS 0.0 2.71e-9          !Disk Feed inductance = 2.71 nH
!
! ** ACTIVE FOIL LOAD, ro LENGTH mass rmin
!CYLFOIL 2.0E-2 2.0E-2 9.4E-6 2.0E-3
RLS 0. 0.66E-9          !Can Inductance
!CYLFOIL 1.E-2 6.0E-2 1.33E-6 1.E-3
SPH 0.0025 134. 2.83E-6 .0001
!rinit in m, full angle in degrees, mass in kg, rfinal in m
CSV L2
$ LMICA2
CSV VL2
$VLMICA2
CSV IL2
$ ILMICA2
RCG 0.0 0.0
!
!
!*******Adding the MICA Output Branches********!
BRANCH !MICA1 from A Program
!
TRL LIN 2.0E-9 1.0 1.0 1.E-10          !********************************
TRL LIN 0.75E-9 0.8 1.0 1.E-10          !*******************************
TRL LIN 0.3E-9 2.0 0.8 1.E-10
RLS 0.0 1.0E-9          !Switch Inductance of 1 nH
VENDSOURCE TAB 0.153 0.0          !Source from William Langston Quicksilver
1        0
0        0
1.49E-07        7.19E-01
1.50E-07        9.77E-01
1.51E-07        1.11E+00
1.52E-07        1.00E+00
1.52E-07        8.27E-01
1.53E-07        6.33E-01
1.55E-07        4.58E-01
1.56E-07        2.08E-01
1.57E-07        1.86E-02
1.58E-07        3.04E-01
1.59E-07        5.04E-01
1.61E-07        6.89E-01
1.62E-07        9.60E-01
1.63E-07        1.21E+00
```

1.64E-07	1.01E+00
1.65E-07	8.03E-01
1.67E-07	6.36E-01
1.68E-07	3.87E-01
1.69E-07	1.09E-01
1.70E-07	2.85E-01
1.71E-07	4.60E-01
1.73E-07	6.72E-01
1.74E-07	9.31E-01
1.75E-07	3.25E+06
1.76E-07	3.59E+06
1.77E-07	3.75E+06
1.79E-07	3.85E+06
1.80E-07	3.92E+06
1.81E-07	4.00E+06
1.82E-07	4.08E+06
1.83E-07	4.14E+06
1.85E-07	4.21E+06
1.86E-07	4.28E+06
1.87E-07	4.34E+06
1.88E-07	4.30E+06
1.89E-07	4.17E+06
1.91E-07	4.15E+06
1.92E-07	4.20E+06
1.93E-07	4.23E+06
1.94E-07	4.22E+06
1.95E-07	4.20E+06
1.97E-07	4.21E+06
1.98E-07	4.18E+06
1.99E-07	4.12E+06
2.00E-07	4.07E+06
2.01E-07	3.95E+06
2.03E-07	3.78E+06
2.04E-07	3.68E+06
2.05E-07	3.58E+06
2.06E-07	3.46E+06
2.07E-07	3.34E+06
2.09E-07	3.25E+06
2.10E-07	3.14E+06
2.11E-07	3.07E+06
2.12E-07	2.96E+06
2.13E-07	2.86E+06
2.15E-07	2.79E+06
2.16E-07	2.72E+06
2.17E-07	2.66E+06
2.18E-07	2.58E+06
2.19E-07	2.50E+06
2.21E-07	2.42E+06

2.22E-07	2.38E+06
2.23E-07	2.33E+06
2.24E-07	2.27E+06
2.25E-07	2.26E+06
2.27E-07	2.23E+06
2.28E-07	2.22E+06
2.29E-07	2.23E+06
2.30E-07	2.24E+06
2.31E-07	2.22E+06
2.33E-07	2.22E+06
2.34E-07	2.20E+06
2.35E-07	2.11E+06
2.36E-07	2.07E+06
2.37E-07	2.00E+06
2.39E-07	1.96E+06
2.40E-07	1.98E+06
2.41E-07	1.99E+06
2.42E-07	2.02E+06
2.43E-07	2.09E+06
2.45E-07	2.13E+06
2.46E-07	2.07E+06
2.47E-07	1.98E+06
2.48E-07	1.79E+06
2.49E-07	1.62E+06
2.51E-07	1.53E+06
2.52E-07	1.39E+06
2.53E-07	1.25E+06
2.54E-07	1.13E+06
2.55E-07	9.53E+05
2.57E-07	8.26E+05
2.58E-07	7.87E+05
2.59E-07	6.34E+05
2.60E-07	4.04E+05
2.61E-07	2.68E+05
2.63E-07	1.17E+05
2.64E-07	1.40E+04
2.65E-07	-8.52E+04
2.66E-07	-2.15E+05
2.67E-07	-3.20E+05
2.69E-07	-3.88E+05
2.70E-07	-4.59E+05
2.71E-07	-4.50E+05
2.72E-07	-3.89E+05
2.73E-07	-3.81E+05
2.75E-07	-3.44E+05
2.76E-07	-2.95E+05
2.77E-07	-3.25E+05
2.78E-07	-3.28E+05

```
2.79E-07        -2.97E+05
2.81E-07        -2.65E+05
2.82E-07        -1.81E+05
2.83E-07        -4.76E+04
2.84E-07        4.49E+04
2.85E-07        1.64E+05
2.87E-07        3.24E+05
2.88E-07        3.91E+05
2.89E-07        4.63E+05
2.90E-07        5.35E+05
2.91E-07        6.20E+05
2.93E-07        6.94E+05
2.94E-07        7.94E+05
2.95E-07        8.62E+05
2.96E-07        9.66E+05
2.97E-07        1.16E+06
2.99E-07        1.27E+06
3.00E-07        1.38E+06
4.00E-07        0.0
Last-entry
!
BRANCH !MICA2 from Program A
!
TRL LIN 1.5E-9 1.0 1.0 1.E-10
TRL LIN 0.65E-9 0.8 1.0 1.E-10
TRL LIN 0.23E-9 2.0 0.8 1.E-10
RLS 0.0 1.0E-9          !Switch Inductance of 1 nH
!
VENDSOURCE TAB 0.153 0.0        !Source from William Langston Quicksilver
1       0
0       0
1.49E-07        1.62E+00
1.50E-07        1.71E+00
1.51E-07        9.03E-01
1.52E-07        1.81E-02
1.52E-07        -3.37E-01
1.53E-07        -5.21E-01
1.55E-07        -7.24E-01
1.56E-07        7.13E-02
1.57E-07        1.02E+00
1.58E-07        1.45E+00
1.59E-07        1.86E+00
1.61E-07        9.76E-01
1.62E-07        1.13E-01
1.63E-07        -5.43E-01
1.64E-07        -7.00E-01
1.65E-07        6.97E-02
1.67E-07        8.18E-01
```

1.68E-07	1.47E+00
1.69E-07	1.88E+00
1.70E-07	1.22E+00
1.71E-07	3.04E-01
1.73E-07	-2.80E-01
1.74E-07	-9.28E-01
1.75E-07	2.62E+06
1.76E-07	2.92E+06
1.77E-07	3.06E+06
1.79E-07	3.15E+06
1.80E-07	3.22E+06
1.81E-07	3.29E+06
1.82E-07	3.36E+06
1.83E-07	3.42E+06
1.85E-07	3.49E+06
1.86E-07	3.56E+06
1.87E-07	3.63E+06
1.88E-07	3.55E+06
1.89E-07	3.51E+06
1.91E-07	3.54E+06
1.92E-07	3.60E+06
1.93E-07	3.67E+06
1.94E-07	3.72E+06
1.95E-07	3.74E+06
1.97E-07	3.81E+06
1.98E-07	3.86E+06
1.99E-07	3.90E+06
2.00E-07	3.95E+06
2.01E-07	3.92E+06
2.03E-07	3.79E+06
2.04E-07	3.79E+06
2.05E-07	3.79E+06
2.06E-07	3.78E+06
2.07E-07	3.78E+06
2.09E-07	3.72E+06
2.10E-07	3.69E+06
2.11E-07	3.68E+06
2.12E-07	3.62E+06
2.13E-07	3.57E+06
2.15E-07	3.52E+06
2.16E-07	3.37E+06
2.17E-07	3.29E+06
2.18E-07	3.24E+06
2.19E-07	3.14E+06
2.21E-07	3.06E+06
2.22E-07	3.03E+06
2.23E-07	2.96E+06
2.24E-07	2.92E+06

2.25E-07	2.87E+06
2.27E-07	2.80E+06
2.28E-07	2.78E+06
2.29E-07	2.76E+06
2.30E-07	2.73E+06
2.31E-07	2.67E+06
2.33E-07	2.55E+06
2.34E-07	2.36E+06
2.35E-07	2.14E+06
2.36E-07	1.97E+06
2.37E-07	1.82E+06
2.39E-07	1.69E+06
2.40E-07	1.55E+06
2.41E-07	1.42E+06
2.42E-07	1.21E+06
2.43E-07	1.09E+06
2.45E-07	1.01E+06
2.46E-07	8.86E+05
2.47E-07	7.82E+05
2.48E-07	6.74E+05
2.49E-07	5.42E+05
2.51E-07	4.48E+05
2.52E-07	3.58E+05
2.53E-07	2.45E+05
2.54E-07	2.16E+05
2.55E-07	1.85E+05
2.57E-07	1.91E+05
2.58E-07	2.46E+05
2.59E-07	2.97E+05
2.60E-07	3.44E+05
2.61E-07	3.57E+05
2.63E-07	3.32E+05
2.64E-07	2.82E+05
2.65E-07	2.63E+05
2.66E-07	2.40E+05
2.67E-07	1.84E+05
2.69E-07	1.93E+05
2.70E-07	2.56E+05
2.71E-07	2.84E+05
2.72E-07	3.07E+05
2.73E-07	2.70E+05
2.75E-07	2.20E+05
2.76E-07	2.36E+05
2.77E-07	3.05E+05
2.78E-07	3.32E+05
2.79E-07	3.78E+05
2.81E-07	4.23E+05
2.82E-07	3.54E+05

```
2.83E-07      3.46E+05
2.84E-07      4.39E+05
2.85E-07      4.94E+05
2.87E-07      5.39E+05
2.88E-07      6.26E+05
2.89E-07      6.88E+05
2.90E-07      7.67E+05
2.91E-07      8.78E+05
2.93E-07      9.17E+05
2.94E-07      1.01E+06
2.95E-07      1.13E+06
2.96E-07      1.18E+06
2.97E-07      1.20E+06
2.99E-07      1.21E+06
3.00E-07      1.17E+06
4.00E-07      0.
Last-entry
!
!
!
=================================================================
===
! E N D O F S I M U L A T I O N
```

DISTRIBUTION

2	M2497	Central Technical Files, 8944
2	MS0899	Technical Library, 4536
3	MS1196	Tom Nash, 1677
1	MS1194	Dillon McDaniel, 1650
1	MS0125	Pace Vandevender, 12101